Received: 4 August 2024 | Revised: 26 November 2024 | Accepted: 16 December 2024

DOI: 10.1002/jev2.70031

RESEARCH ARTICLE

A simple polydopamine-based platform for engineering extracellular vesicles with brain-targeting peptide and imaging probes to improve stroke outcome

Xiaojing Shi[1,2] | **Lu Zhang**[3] | **Shengju Wu**[1] | **Chunfu Zhang**[1] | **Muyassar Mamtilahun**[1] | **Yongfang Li**[4] | **Zhijun Zhang**[1] | **Changjing Zuo**[3] | **Fengzhen Cui**[1] | **Wanlu Li**[1] | **Guo-Yuan Yang**[1] | **Yaohui Tang**[1]

[1]Shanghai Jiao Tong University Affiliated Sixth People's Hospital, School of Biomedical Engineering, Shanghai Jiao Tong University, Shanghai, China

[2]McGovern Institute for Brain Research, Massachusetts Institute of Technology, Cambridge, Massachusetts, USA

[3]Department of Nuclear Medicine, Changhai Hospital Affiliated to Naval Medical University, Shanghai, China

[4]Department of Rehabilitation Medicine, Ruijin Hospital, Shanghai Jiao Tong University, Shanghai, China

Correspondence
Yaohui Tang, Shanghai Jiao Tong University Affiliated Sixth People's Hospital, School of Biomedical Engineering, Shanghai Jiao Tong University, 1954 Hua Shan Road, Shanghai 200030, China.
Email: yaohuitang@sjtu.edu.cn

Funding information
National Natural Science Foundation of China, Grant/Award Numbers: 82371307, 81901804, 82172529, 82472590, 82271320; National Key Research and Development Program of China, Grant/Award Number: 2022YFA1603600; Fundamental Research Funds for the Central Universities, Grant/Award Number: YG2023ZD02; Shanghai Municipal Education Commission, Grant/Award Number: ZXWH1082101; Shanghai Sailing Program, Grant/Award Number: 23YF1420700

Abstract

Extracellular vesicles (EVs) have shown great potential for treating various diseases. Translating EVs-based therapy from bench to bedside remains challenging due to inefficient delivery of EVs to the injured area and lack of techniques to visualize the entire targeting process. Here we developed a dopamine surface functionalization platform that facilitates easy and simultaneous conjugation of targeting peptide and multi-mode imaging probes to the surface of EVs. Utilizing this platform we concurrently modified M2 microglia-derived EVs (M2-EVs) with neuronal targeting peptide rabies virus glycoprotein peptide 29 (RVG29) and multi-modal imaging tracers, resulting in the targeted delivery of M2-EVs to stroke mice brain and enabled the dynamic visualization of the targeting process from whole-body to cellular levels. We determined that intra-arterial injection achieved the highest efficiency of targeted delivery of engineered EVs to the stroke mice brain, improved therapeutic efficacy by reducing neuronal apoptosis. Mechanistically, EVs miRNA array revealed that a number of anti-apoptosis related miRNAs were significantly up-regulated, including miR-221-3p and miR-423-3p, both exerted anti-apoptotic effects through p38/ERK signalling pathways in stroke. Overall, this platform provides a facile and powerful tool for multifunctional engineering of EVs for multiscale therapeutic evaluation and enhancement of EV-based therapy, with valuable prospects for clinical translation.

KEYWORDS
extracellular vesicle, Ischemic stroke, Multifunctional engineering, Targeted delivery

Xiaojing Shi, Lu Zhang and Shengju Wu contributed equally to this study.

1 | INTRODUCTION

The therapeutic application of extracellular vesicles (EVs) has been greatly propelled by the promising preclinical results in areas such as cancer, cardiovascular diseases and neurodegenerative diseases (Colvett et al., 2023; Wang et al., 2023). However, the limited targeting ability of EVs to injury areas severely hampers their clinical translation (Liu et al., 2022). Enhancing targeted delivery of EVs to injury areas as well as dynamically visualizing the targeting process are crucial for further improving their therapeutic potential.

To overcome these challenges, the engineering EVs for targeted delivery and noninvasive, reproducible, facile and quantitative monitoring are urgently needed (Shi et al., 2023). Current engineering strategies include genetic engineering and chemical modification. Genetic engineering fuses the gene sequence of a guiding or tracer protein with that of a selected EV membrane protein. This approach is effective for surface display of peptides and proteins; however, it is limited to targeting genetically encodable motifs. In addition, any genetic manipulation could hinder clinical approval EVs due to safety issues. Chemical modification allows a wide range of ligands or tracer elements directly added to the reactive group on the EV membrane via conjugation reactions or lipid assembly (Gonzalez et al., 2021; Zhang et al., 2020). However, the complexity of the surface may reduce the efficiency of the reaction, and this covalent modification always requires toxic chemicals to induce or catalyze the bonds, which could lead to structural, surface electrode potential and functional alterations of EVs. In addition, directly conjugating EVs with imaging tracers such as ^{125}I via physical absorption is very straightforward (Banks et al., 2020), but the labelling is unstable, and easily detaches from EVs under physiological conditions. Encapsulating targeting proteins and the tracer molecules into EVs using electroporation (Pan et al., 2020) or sonication (Jang et al., 2021) could disrupt EVs membrane and significantly decrease the contents of protein and RNA within EVs. Therefore, a simple but powerful method to simultaneously enhance their targeting capability as well as label EVs without affecting their biological activity is highly desirable.

In recent years, polydopamine (PDA), a mussel-inspired adhesive protein has attracted extensive interest for its self-polymerization property and versatile chemical reactivity, making it a designable coating material for theranostic construction (Yang et al., 2016). Unlike other sophisticated engineering methods, PDA coating can be easily prepared by gently stirring under slightly alkaline conditions, enabling the formation of a thin but robust layer on the EV surface. The catechol-to-catechol coupling in PDA coating readily coordinates with various imaging or therapeutic metal ions, such as Fe^{3+} (Zhang, Si et al., 2021), Gd^{3+} (Lemaster et al., 2019) and Pt^{4+} (Zhang et al., 2016). PDA can also react with halogen, thiols or amines via Schiff base or Michael addition reactions, which facilitates the modification of EVs with radioisotopes, anti-biofouling polymers or monolayers and further functionalizes them with targeting molecules (Zhang, Wu et al., 2021). Additionally, PDA could scavenge reactive oxygen species (ROS) in physiological condition, so this method also serves to protect the EVs membrane from harsh environments not only during the labelling process but also under hypoxic or ischemic conditions (Xu et al., 2023).

Based on these unique properties of PDA, we established a PDA-functionalized platform that allows for engineering multiple functional units on the surface of M2 microglia-derived EVs (M2-EVs) with targeting peptide rabies virus glycoprotein 29 (RVG29), which has been previously shown to target neurons by binding to the nicotinic acetylcholine receptor (nAChR) (Kumar et al., 2007; Kwon et al., 2016), and imaging agents like superparamagnetic iron oxide (SPIO), radioactive ^{125}I and fluorescent dyes for different purposes. BV2 cells are a widely used microglial cell line that exhibits morphological and functional similarities to primary microglia (Guan et al., 2024). They are particularly advantageous for in vitro studies due to their ease of culture and genetic manipulation. Moreover, BV2 microglia can be polarized towards an M2 phenotype, which acquires anti-inflammatory and neuroprotective properties (Song et al., 2019). Our previous studies have widely explored the effects of M2 BV2 microglia derived EVs on stroke. We demonstrated that EVs from M2 BV2 microglia reduced infarct volume and glial scar formation (Li, Song et al., 2021; Song et al., 2019), as well as promoted white matter repair (Li et al., 2022), suggesting its significant role in stroke treatment and translational potential. Thus, EVs from M2 microglia were used in our study. Utilizing this multifunctional approach we enhanced the neuronal targeting capability of EVs, and maximally achieved in vivo real-time visualization of EVs at whole-organism, organ/tissue, cellular and molecular levels, further promoted therapeutic efficacy for stroke. Overall, our study suggested that PDA-coating strategy provides a powerful and adaptable platform for enhancing EV targeting and therapeutic efficacy in stroke, with potential applications in other therapeutic contexts and clinical translation in the future (Figure 1).

2 | MATERIALS AND METHODS

2.1 | M2 BV2 cell activation

Mouse microglial cell line (BV2 cells) were cultured using Dulbecco's modified Eagle medium (DMEM, HyClone, Logan, UT) with 7% inactivated foetal bovine serum (FBS, Gibco) and 1% penicillin/streptomycin antibiotic (Meilunbio, China). BV2 cells were treated with interleukin-4 (IL-4) at 20 ng/mL for 48 h to polarize to M2 BV2 cells (Song et al., 2019). Cells were cultured in a humidified incubator at 37°C with 5% CO_2. M2 BV2 cells were further identified using immunostaining and qPCR.

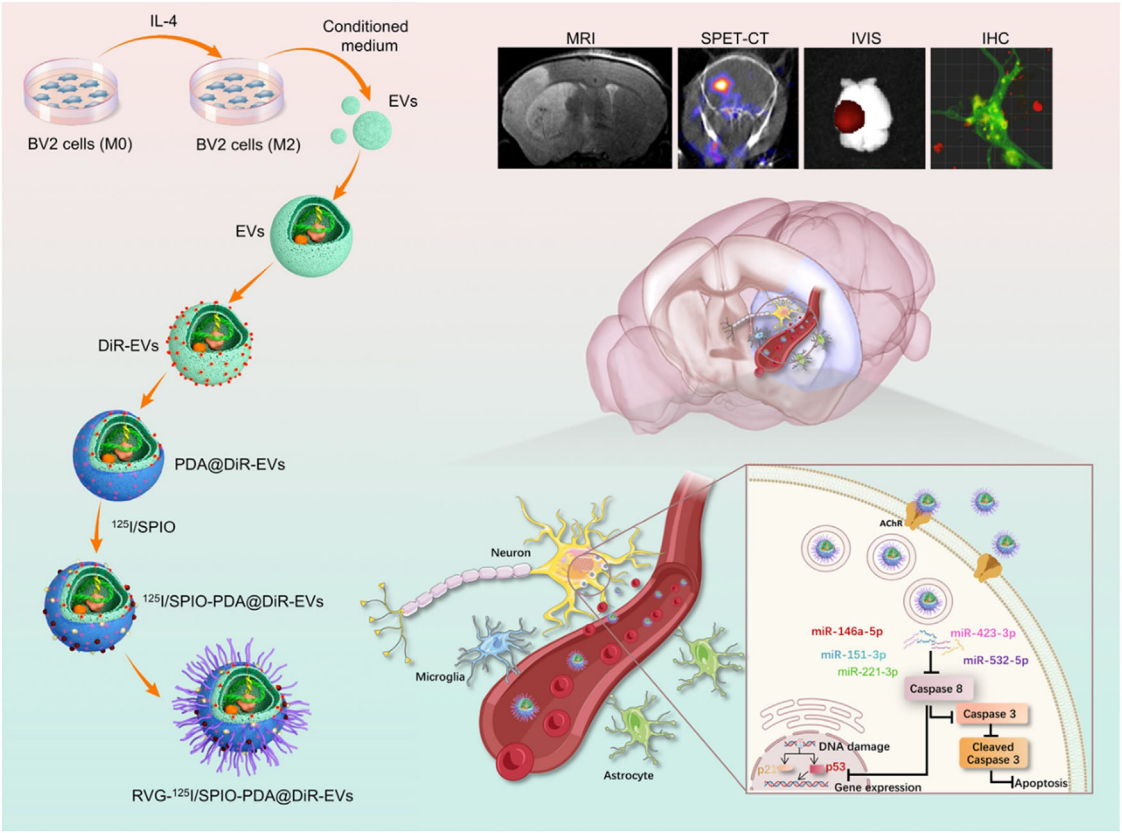

FIGURE 1 By leveraging the multifunctionality of PDA, we developed a PDA-functionalized platform that could simultaneously label M2-EVs with the neuronal targeting peptide RVG29 and multi-modal imaging tracers in a very simple manner. This platform not only enhances the neuronal targeting capability of EVs but also enables us to visualize the targeting process from whole-body to cellular levels through SPECT/MRI/Fluorescent imaging. Intra-arterial administration of such engineered extracellular vesicles during the ultra-acute stage of stroke yields optimal therapeutic efficacy. In addition, through miRNA-seq analysis, we identified miR-221-3p and miR-423-3p were enriched in M2 EVs and they exerted anti-apoptotic effects through p38/ERK signalling pathways. EV, extracellular vesicle; M2-EV, M2 microglia-derived EV; PDA, polydopamine; RVG29, rabies virus glycoprotein peptide 29.

2.2 | qPCR

Total RNA from the BV2 cells was isolated using TRIzol Reagent (Invitrogen, Carlsbad, CA, USA). RNA concentration was examined using a spectrophotometer (NanoDrop 1000, Thermo Fisher) followed by a reverse transcription process using cDNA Synthesis SuperMix Kit (Yeason, China) under the following conditions: 42°C for 1 h and then 95°C for 5 min. SYBR Green Master Mix (11203ES08Yeason) was used to perform real-time PCR. A two-stage amplification reaction was conducted under the following conditions: 95°C for 5 min, followed by 40 cycles at 95°C for 10 s and 60°C for 30 s. The primer sequences were:

CD206 forward primer: 5′- CAGGTGTGGGCTCAGGTAGT-3′, reverse primer: 5′- TGTGGTGAGCTGAAAGGTGA-3′.

Arginase (ARG) forward primer: 5′- GGAACCCAGAGAGAGCATGAG-3′, reverse primer: 5′- CTCGAGGCTGTCCTTTTGAGA-3′.

TNF-α forward primer: 5′- ACCCTCACACTCAGATCATCTT-3′, reverse primer: 5′- GGTTGTCTTTGAGATCCATGC-3′.

Interleukin-1 (IL-1) forward primer: 5′- CGCAGCAGCACATCAACAAGAGC-3′, reverse primer: 5′- TGTCCTCATCCTGGAAGGTCCACG-3′.

GAPDH forward primer: 5′- GAGGGATGCTGCCCTTACC-3′, reverse primer: 5′- AAATCCGTTCACACCGACCT-3′.

2.3 | EV isolation and identification

EVs were isolated from the supernatant of the M2 BV2 cells. EV-free FBS was prepared by ultracentrifugation of FBS (Gibco) at 100,000 × *g* for 70 min to remove EVs from the serum. Prior to collecting the culture medium, BV2 cells were thoroughly washed with PBS and subsequently cultured in EV-free medium, which consisted of DMEM supplemented with 1% penicillin/streptomycin and 7% EV-free FBS, for 36–48 h. The supernatant was collected and underwent sequential centrifugation at 300 × *g* for 10 min, 2000 × *g* for 15 min, 10,000 × *g* for 30 min and ultracentrifugation at 100,000 × *g* for 70 min at 4°C. The

EVs were washed once with PBS at 100,000 × *g* for 70 min and suspended for further characterization. A transmission electron microscope (TEM) at an accelerating voltage of 120 kV (Thermo Scientific, Waltham, MA, USA) was used to identify the structure of the EVs. Nanoparticle tracking analysis (NTA, Brookhaven, New York, USA) was used to measure EVs diameter and particle number. The protein content was measured using BCA protein assay (Thermo Scientific). EV markers CD63 and tumour susceptibility gene 101 (TSG101) were examined by Western blot analysis, and total protein was detected by Coomassie brilliant blue staining.

2.4 | EVs labelling and characterization

2.4.1 | Fluorescent dye labelling

Near-infrared fluorescent dye, DiR (MB12482, Meilunbio, China) and red fluorescent dye, PKH26 (MINI26, Sigma-Aldrich, MO, USA) were used according to the instructions with modification (Puzar Dominkus et al., 2018). For in vivo and ex vivo studies, EVs were incubated with 1 μM DiR solution at 37°C for 5 min. For in vitro uptake assay, EVs were labelled with PKH26 (1:500 dilution) for 5 min at room temperature. EVs-free FBS was added to stop excess labelling. The labelled EVs were washed in PBS at 100,000 × *g* for 1 h, and the pellet was suspended in PBS for further use.

2.4.2 | PDA coating

Two hundred microlitres of EVs were mixed with PBS (1:1), 1 mg PDA dissolved in 8 mL Tris-Buffer (pH = 8.5) was added to the solution and reacted for 10 min. After that, PDA-coated EVs were suspended in dialysis tubes (100 kDa MWCO), separated by ultrafiltration at 10,000 × *g* for 8 min, and then washed with PBS three times. PDA was linked with amino-functionalized indocyanine green (ICG) to evaluate the labelling efficiency. The fluorescence intensity of ICG-PDA@EVs was measured before and after ultrafiltration with a Microplate Reader (Synergy2, Biotek, USA). TEM, NTA, Western blot and Coomassie blue staining were performed to examine the EVs before and after PDA coating.

2.4.3 | SPIO labelling

PDA@EVs were labelled with amino-functionalized SPIO (Sigma, 725331) at a concentration of 20 μg/mL for 1 h, and then washed and ultrafiltered to discard excess SPIO particles. To examine the labelling stability of SPIOs, the SPIO-PDA@EVs were suspended in DMEM high glucose containing 10% FBS at 37°C and the detached SPIO particles were measured at 0-, 1-, 3-, 6-, 12-, 24- and 48-h with an inductively coupled plasma optical emission spectrometer (ICP-OES, ICAP-6300, Thermo Fisher). For relaxometry of SPIO-labelled EVs, deionized water, water suspension of SPIO particles, water-diluted SPIO-PDA@EVs (≈1.0×10^5 particles mL^{-1}) were evaluated using a 1.41 T minispec mq60 NMR Analyzer (Bruker, Germany). Briefly, 300 μL of SPIO-PDA@EVs dilutions were filled into the test tubes and T2 relaxation time were measured using a standard Carr-Purcell-Meiboom-Gill pulse sequence at 37°C. The T2 relaxivities were determined by a linear fit of the inverse relaxation times as a function of the iron concentrations (Xu et al., 2009). The possible release of SPIO from the probes was studied in triplicate by co-incubating 1.0×10^9 of the probes in 5 mL of DMEM high glucose containing 10% FBS at 37°C for different periods. After incubation, the probes were collected by ultrafiltration and the free SPIO in the serum was measured by ICP-OES. The stability of SPIO was expressed as a percentage of SPIO retained on PDA@EVs to the total amount of SPIO on the probes. Zeta potentials of labelled EVs at each step during probe preparation were measured using dynamic light scattering (DLS) (Nano Zetasizer, Malvern, UK). To evaluate the stability of SPIO labelling, the hydrodynamic diameter and superficial charge of bare EVs, PDA@EVs and SPIO-PDA@EVs were examined in 10% FBS (v/v) solution at 0-, 1-, 2-, 3- and 4- days by DLS.

2.4.4 | Radionuclide labelling

Radioactive ^{125}I labelling was achieved by a classical Iodogen-catalyzed method. The PDA@EVs suspension (0.5 mL, ≈1.2×10^{11} particles mL^{-1}) was added to a glass tube with a bottom coating with 20 μg Iodogen. Freshly prepared $Na^{125}I$ solution (500 μCi, 18.5 Mbg) was added into the tube, which was intermittently oscillated to avoid the sedimentation of PDA@EVs. After incubation at room temperature for 30 min, the final products were purified through ultracentrifuge and washed with PBS three times. Radio-thin-layer chromatography with a γ-detector (RTLC; AR2000, Bioscan, USA) was performed to evaluate the labelling efficiency. The stability of the radioactive probe was assessed by co-incubating 5 μL of the sample in 200 μL of 10% FBS in DMEM high glucose at 37°C for different periods (0-, 1-, 3-, 6-, 12- and 24-h). After incubation, the probes were collected by centrifugation

and the radioactivity retained on the particles was counted. Chromatography paper and 0.9% NaCl were used as stationary and mobile phases. The radiochemical purity of ^{125}I was expressed as a percentage of radioactivity retained on PDA@EVs to the radioactivity of the probes.

2.4.5 | ICP-OES measurement

To evaluate the stability of SPIO labelling, 100 μL of SPIO was added to PDA@EVs that had been treated with PDA for 45 min and allowed to react for 5 min. The resulting SPIO-PDA@EVs were suspended in DMEM high glucose containing 10% FBS and incubated at 37°C for 48 h. Labelling stability was assessed by measuring the Fe content of the SPIO-PDA@EVs using an ICP-OES (ICAP-6300, Thermo Fisher) following the addition of KI, ultracentrifugation and dilution with deionized water. Additionally, the Fe content of SPIO-PDA@EVs ($\approx 3.8 \times 10^{12}$ particles mL-1) and an equivalent amount of pure SPIO were compared after heating at 120°C with gold nitrate elimination for 1 h. The labelling rate was calculated as Fe in SPIO-PDA@EVs/Fe in total SPIO X 100%.

2.4.6 | EV analysis with Exoview

The ExoView Tetraspanin chip (ExoView, Boston, MA, USA) is utilized for the identification of EVs through its array of antibodies specifically targeted against the tetraspanin proteins CD81 and CD9. Mouse IgG1 was utilized as a negative control, with 35 μL of sample applied to the chip surface and incubated overnight. Post-washing, the chips were subjected to incubation with ExoView Tetraspanin Labelling ABs (EV-TC-AB-01), comprising a cocktail of fluorescently-tagged antibodies specific to CD63 conjugated with ALEXA 647, CD81 with ALEXA 555 and CD9 with ALEXA 488, for the purpose of co-localization assays aimed at the identification of EVs. Subsequently, the chips were imaged using the ExoView R100 reader (ExoView), which employs single particle interferometric reflectance imaging sensor (SP-IRIS) technology coupled with ExoScan v0.998 (ExoView) acquisition software for data capture, with size thresholds for EV identification specifically defined within a range of 50 to 200 nm in diameter.

2.4.7 | STEM imaging

The imaging of SPIO-PDA@EVs was performed using a scanning transmission electron microscope (STEM, Talos F200X G2, Thermo Scientific) at the Center of Instrumental Analysis at Shanghai Jiao Tong University. To prepare the sample, 5 μL of SPIO-PDA@EVs was placed on a hydrophilic carbon film and incubated for 2 min. The sample on the copper mesh was washed with deionized water three times and dried at room temperature for 10 s each time to reduce salt. Next, 4 μL of phosphotungstic acid was added to the sample and dried for 1 min. To prevent the SPIO-PDA@EVs from entering the pole shoe, a carbon film was placed on top of the sample. Bright-field and high-angle annular dark-field (HAADF) imaging were performed for 5–10 min using either weight percentage (wt%) or atomic percentage (at%) scanning. For energy dispersive spectrometer detector (EDS) mapping analysis, the pretreatment process of SPIO-PDA@EVs was the same as STEM. The mapping analysis of ferrum, iodine, nitrogen, carbon and oxygen elements was completed by the same sample of STEM and compared.

2.4.8 | RVG29 peptide modification

For RVG29 peptide conjugation, 50 μg of the peptide was added to the EVs suspension (300 μL) and reacted for 2–4 h at room temperature. Then the peptide-conjugated EVs were purified by ultrafiltration and washed with PBS. The fluorescence intensity of FITC-RVG-PDA@EVs was quantified before and after purification using Microplate System to evaluate the conjugation rate.

2.5 | Neuronal cell culture

Mouse neuronal cell line, Neuro-2a cell lines were purchased from the Cell Bank of Chinese academic institute (Shanghai, China). Primary neurons were prepared from cerebral cortices of neonatal 24-h-old mice. Briefly, dissociated cortical cells were spread on glass slides pre-coated with poly-D-lysine (Sigma-Aldrich) and cultured in DMEM at a density of 7.0×10^5 cells per well. After 4 h of seeding, the cells were washed with PBS and added with Neurobasal A medium (Gibco, Carlsbad, NM, USA) supplemented with 1% B-27 (Gibco) and 0.5% P/S. Cultures were used for experiments 7 to 10 days after seeding.

2.6 | In vitro uptake and cell viability assay

To determine the concentration of free RVG29 competing for uptake assay, Neuro-2a cells (6×10^5 cells per well) were treated with 3.75, 7.5, 15 and 30 μg/mL free RVG29 peptide for 30 min, then washed with PBS twice, and incubated with 10 μg/mL RVG-modified EVs for 12 h. After that, cultures were checked under a fluorescent microscope. The percentage of cells with $PKH26^+$ EVs localized in the cytoplasm was calculated. For in vitro uptake assay, EVs were pre-labelled with PKH26. Co-culture of primary neurons and glial cells was incubated with a medium containing EVs, PDA@EVs, RVG-PDA@EVs or RVG-PDA@EVs plus free RVG29 peptide at the concentration of 10 μg/mL (5.1×10^9 particles mL^{-1}) for 12 h. For the competing RVG group, co-culture was pretreated with 15 μg/mL RVG29 solution for 30 min and washed with PBS twice. After the incubation, cell slides were collected and fixed in 4% PFA for immunostaining. The phagocytic index (PI) was introduced to quantify the phagocytic ability of cells, calculated as Percent of phagocytic cells × Number of phagocytic particles (Sano et al., 2003). To study the effects of different EV probes on cell viability, primary neurons (1.0×10^4 per well) were cultured in 96-well plates and treated with 10 μg/mL EVs, PDA@EVs, RVG-PDA@EVs, RVG-PDA@EVs plus free RVG29 for 6 h. After the incubation, the neuron viability was evaluated by the Cell Counting Kit-8 (MA0218, Meilunbio, China) according to the manufacturer's instructions. Absorbance was measured at a wavelength of 450 nm.

2.7 | Animal experimental design

Adult male ICR mice (8 weeks, 25–27 g weight) and neonatal ICR mice were purchased from JSJ Laboratory (Shanghai, China). Animal studies were reported under Animal Research: Reporting in vivo Experiments: ARRIVE guidelines. The procedure for using laboratory animals was approved by the Institutional Animal Care and Use Committee (IACUC) of Shanghai Jiao Tong University, Shanghai, China (Permission number: 2020033). For multi-model imaging, mice that underwent transient middle cerebral artery occlusion (tMCAO) surgery were randomly divided into three groups, including (1) Intra-arterial (i.a.) injection group: EVs were injected through the carotid artery; (2) Intravenous (i.v.) injection group: EVs were injected through the tail vein; (3) Intra-nasal (i.n.) injection group: EVs were injected through the nasal. One day after middle cerebral artery occlusion (MCAO), 100 μg (1.0×10^{11} particles, 50–100 μL) M2-EVs were transplanted into ischemic mice via i.a., i.v., or intranasal injection. For EVs-based therapy, mice were randomly divided into three groups and received treatments, including PBS, M2-EVs and RVG-modified M2-EVs after stroke.

2.8 | A mouse model of middle cerebral artery occlusion

The surgery of MCAO was performed as described previously (Mamtilahun et al., 2021). Adult mice ($n = 90$) were anesthetized with 1.5%-2% isoflurane and 30%/70% oxygen/nitrous oxide. Body temperature was maintained at 37°C using a heating pad. Briefly, the common carotid, internal and external carotid arteries were separated. A 6-0 suture (Covidien, Mansfield, MA, USA) coated with silicon (Heraeus Kulzer, Germany) was inserted from the external carotid artery (ECA), followed by the internal carotid artery (ICA), and gently stopped at the opening of the middle cerebral artery (MCA). The success of occlusion was determined by monitoring the decrease in surface cerebral blood flow (CBF) to 10% of baseline CBF using a laser Doppler flowmetry (Moor Instruments, Devon, UK). Reperfusion was performed by withdrawing the suture 90 min after MCAO.

2.9 | MR imaging

MR imaging was conducted using a 7T MRI scanner (Biospec System 70/20, Bruker, Germany) using a T2-weighted spin−echo sequence with the following parameters: (repeat time (TR) = 2500 ms, echo time (TE) = 33 ms, field of view (FOV) = 20 × 20 mm, matrix = 256 × 256 and slice thickness = 700 μm. Immediately after the final in vivo imaging, mice were sacrificed, and the brain was collected and fixed in 4% paraformaldehyde solution for histological analysis.

2.10 | Prussian blue staining

Cellular iron accumulation was detected by Prussian Blue Iron Stain Kit (60533ES20, Yeasen, China) according to the manufacturer's instructions. Frozen mouse brain slices were washed three times by ddH_2O and fixed with PFA for 15 min. Mix Prussian stain B (potassium ferrocyanide solution) and C (acid solution) 1:1, and then add them to brain slices for incubation at room temperature for 30 min until iron ions were evaluated. After that, samples were continuously rinsed with water for 5 min and

stained for 5 min with Nuclear Fast Red solution. Finally, rinse with water for 5 s to remove excess dye and seal with neutral gum. Samples were imaged under a light microscope (Leica). The iron levels were determined based on the colour intensities measured by ImageJ.

2.11 | SPECT/CT imaging

For SPECT/CT imaging, mice were injected with ^{125}I-labelled EVs and imaged at 0.5-, 6-, 24- and 48-h post-injection, at a radiation dosage of 300 μCi each mouse. The amount of ^{125}I-PDA@EVs was measured by the density of injected dose per volume of organs from a region of interest (ROI). SPECT/CT scans were obtained using a small-animal imaging system (Bioscan). The CT images provided anatomical references to the mouse's location. The SPECT images were obtained at 32 projections over 360°C (radius of rotation = 7.6 cm, 30 s/projection). Reconstructed data from SPECT and CT were visualized and co-registered using InVivoScope (Bioscan). ROIs were drawn in major organs that presented obvious radioactivity. The concentration of radioactivity (μCi/mm^3) was generated by the software for each ROI. For ex vivo distribution study, prior to injection, total radioactivity of injected EVs were measured as counts per minute (CPM) (60 s) using a well-type scintillation detector (SN-6100, Shanghai). After imaging, the organs of interest (including brain, heart, liver, etc.) were harvested, weighed and the respective radioactive signal was quantified in the same way. CPM in the air was used as a blank control. The %ID/g of each organ was calculated using the following formula: 100 × (CPM in organ/total injected CPM)/(organ weight in gram).

2.12 | Fluorescence imaging and ex vivo biodistribution

For in vivo fluorescence imaging, mice were injected with DiR-labelled EVs and imaged at 0.5-, 6-, 24- and 48-h post-injection using the IVIS system at excitation and emission wavelengths of 748 and 780 nm, respectively. ROI for the ipsilateral and contralateral brain, heart, lung, stomach, liver, spleen, kidney and background were selected from equivalent-sized areas containing the same number of pixels. Quantification of uptake was determined by drawing ROIs for each organ. Animals were sacrificed 48 h post-injection; immediately after imaging, the ipsilateral and contralateral brain, heart, lung, stomach, liver, spleen and kidney were extracted and stored on ice. Dissected organs were weighed in tared tubes and imaged. Fluorescence in organs was expressed as mean fluorescence or signal/area using arbitrary units (AU).

After imaging, organs were weighed and stored at −80°C for homogenization and subsequent analysis. Homogenization was performed as described by the previous study with some modifications (Oliveira et al., 2012). Briefly, 80–150 mg of each organ was added to 1 mL of lysate buffer (with 1× RIPA buffer containing 50 mM Tris-HCl, 150 mM NaCl, 1% Ige pal (NP40), 0.5% Na-deoxycholate, 0.1% SDS and 1% protease inhibitor cocktail; Roche). Then samples were homogenized and centrifuged to collect the supernatant. One hundred microlitres of homogenate was added into black 96-well opaque microplates. The fluorescence intensity in each well was immediately measured. The total fluorescence intensity of the whole organs at the ROI was also quantitatively analyzed with the IVIS system. Mean fluorescence (signal) per gram of tissue was calculated.

For RVG29 competitive binding experiments, free RVG29 peptide (50 μg per mouse) was first administered to the stroke mice 30 min prior to RVG-modified EVs, and then in vivo SPECT/CT and fluorescence imaging were conducted at different time points. After imaging, the mouse brains were harvested, and respective radioactive or fluorescent signal was measured.

2.13 | Immunostaining

At 3 days after MCAO, mice were sacrificed and perfused with PBS followed by 4% paraformaldehyde (PFA, Sinopharm Chemical Reagent, China). Brain samples were removed, fixed in 4% PFA for 2 h, fully dehydrated in 30% sucrose for 2 days at 4°C, then frozen at −80°C. Histological cryosections (30 μm in thickness) from anterior commissure to hippocampus were collected, incubated with 0.3% Triton-100 (Sigma, St Louis, MO) and blocked with 0.1% bovine serum albumin (BSA, Gbico, MA, USA), then incubated with goat anti-Iba-1 (1:200, NB100-1028, novusbio, CO), goat anti-GFAP (1:400, ab53554, Abcam, CA, USA), mouse anti-ARG (1:200, SC-271430, Santa Cruz, CA, USA), rabbit anti-CD206 (1:200, 24595, CST, MA, USA), goat anti-CD31 (1:200, AF3628, R&D), mouse anti-MAP2 (1:200, MAB3418, Millipore) at 4°C overnight. After rinsing with PBS three times, the brain sections were incubated with the secondary antibodies: Alexa Fluor 488-conjugated donkey anti-goat, Alexa Fluor 594-conjugated donkey anti-goat, Alexa Fluor 488-conjugated donkey anti-rabbit, or Alexa Fluor 594-conjugated donkey anti-rat (1:400, Invitrogen, CA, USA) for 1 h at room temperature. One-step TUNEL Apoptosis Assay Kit (MA0224-2, Meilunbio, China) was used for cell death detection. Then the brain sections were rinsed with PBS three times and incubated with DAPI (Life Technologies, Mulgrave, VIC, Australia) for 5 min at RT. After rinsing with PBS, the brain sections were covered and sealed with a mounting medium (Vector Labs, Burlingame, CA, USA). Images were acquired using a confocal microscope (Leica, Wetzlar, Germany).

2.14 | Western blotting

For Western blot, the mice were perfused with PBS, and the whole brain was rapidly removed and placed in a cold mouse brain matrix. The brain was cut into a 2 mm-thick slice before and behind the centre of Willis Circle. Then the striatum region of the brain was separated and transferred into precooled protein lysis buffer (RIPA with protease cocktail inhibitor and phosphatase inhibitor) to extract protein. To extract EV protein, the EVs were lysed in precooled protein lysis buffer (RIPA with protease cocktail inhibitor and phosphatase inhibitor) on ice for 30 min, followed by centrifugation at 12,000 × *g* for 15 min according to previous study (Morente-Lopez et al., 2021). Then The protein content was then assessed using the micro-BCA assay to determine the concentration for Western blotting analysis. Equal amounts of protein were loaded onto 10% (W/V) SDS-PAGE. The proteins were transferred onto the PVDF membrane (Millipore) and incubated with the primary antibodies of CD63 (1:700, SC-15363, Santa Cruz), TSG101 (1:700, ab83, Abcam), Caspase-3/Cleaved caspase-3 (1:1000, 66470-2-Ig, proteintech), p-p38 (1:1000, 4511, CST), p38 (1:1000, 8690, CST), p-JNK (1:1000, 9255, CST), JNK (1:1000, SC-7345, Santa Cruz), p-ERK (1:1000, 4370, CST), ERK (1:1000, 4695, CST) at 4°C overnight. The membrane was washed in TBST buffer and incubated with HRP-conjugated anti-rabbit or anti-mouse IgG (1:5000, Invitrogen) for 1 h at RT, then reacted with an enhanced chemiluminescence substrate (Meilunbio, Shanghai). The result of chemiluminescence was recorded and semi-quantified using the ImageJ software (NIH, Bethesda, MD, USA).

2.15 | Coomassie brilliant blue staining

After electrophoresis, the whole gel was washed with ultrapure water, then immersed into Coomassie-G working solution (containing 12.5% of 1.0% stock Coomassie-G dye, 50% of methanol, 10% of 10% acetic acid) and incubated at 60 rpm/min for 1 h. After the incubation, the gel was washed with a destaining solution (containing 10% acetic acid and 20% methanol) at 80 rpm/min for 2.5 h. The destaining solution was replaced after 30 min of washing.

2.16 | Neurobehavioral tests

Neurobehavioral tests were performed before and 0-, 1- and 3-days after MCAO surgery by an investigator blinded to the experimental design and treatment.

2.16.1 | mNSS test

A modified neurological severity score (mNSS) test was performed 1 and 3 days after MCAO by an investigator blinded to the experimental design and treatment. The mNSS includes a composite of motor, reflex and balance tests. The severity score was graded on a scale from 0 to 14, in which 0 represents normal, and a higher score indicates a more severe injury (Suo et al., 2023).

2.16.2 | Rotarod test

The rotarod test is used to assess motor coordination and balance alterations. Mice were trained for three consecutive days before surgery. The speed was slowly increased from 20 to 40 rpm in 5 min. Each mouse was given three trials, and the time the mice remained on the accelerating rotating rod was recorded.

2.17 | RNA extraction and library construction

Total EVs RNA was extracted from EVs purified from 120 mL of cell medium per sample. Quantitation of total RNA was carried out using the Nanodrop 2000 (Thermo Fisher Scientific, USA). RNA integrity was assessed by Agilent 2100 Bioanalyzer (Agilent Technology, USA). One microgram total RNA of each sample was used for the small RNA library construction using TruSeq Small RNA Sample Prep Kits (RS-200-0012, Illumina, USA) following the manufacturer's recommendations. Briefly, total RNA was ligated to adapters at each end. Then the adapter-ligated RNA was reverse transcribed to cDNA and performed PCR amplification. The PCR products ranging from 140 to 160 bp were isolated and purified as small RNA libraries. Library quality was assessed on the Agilent Bioanalyzer 2100 system using DNA High Sensitivity Chips. The libraries were finally sequenced using

the Illumina NovaSeq 6000 platform. A total of 150 bp pair-end reads were generated. The miRNA sequencing and analysis of M2-EVs, M0-EVs and RVG-M2-EVs was conducted by OE Biotech (Shanghai, China).

2.18 | Bioinformatic analysis

The basic reads were converted into sequence data by base calling. Low-quality reads were filtered, and the reads with 5′ primer contaminants and poly (A) were removed. The reads without 3′ adapter and insert tag, the reads shorter than 15 nt or longer than 41 nt from the raw data were filtered, and the clean reads were obtained. For the primary analysis, the length distribution of the clean sequences in the reference genome was determined. The clean read sequences were aligned and subjected to the BLAST search against Rfam v.10.1 (http://www.sanger.ac.uk/software/Rfam) and GenBank databases (http://www.ncbi.nlm.nih.gov/genbank/) (Griffiths-Jones et al., 2003). The known miRNAs were identified by aligning against miRBase v22 database (Griffiths-Jones et al., 2008), and the known miRNA expression patterns in different samples were analyzed. After that, unannotated reads were analyzed by mirdeep2 to predict novel miRNAs (Friedlander et al., 2012). Based on the hairpin structure of a pre-miRNA and the miRBase database, the corresponding miRNA star sequence and miRNA mature sequence were also identified. Differentially expressed miRNAs were calculated and filtered with the threshold of p-value < 0.05. While the p-value was calculated with DEG algorithm in the R package for experiment with biological replicates (Wang et al., 2010), and with Audic Claverie statistic for experiment without biological replicates (Tino, 2009). The targets of differentially expressed miRNAs were predicted by using software miranda (Enright et al., 2003), with the parameter as follows: $S \geq 150$ $\Delta G \leq -30$ kcal/mol and demand strict 5′ seed pairing. GO enrichment and KEGG pathway enrichment analysis of differentially expressed miRNA-target-Gene were respectively performed using R based on the hypergeometric distribution.

2.19 | miRNA mimics transfection

Oligo miRNAs were purchased from Obio Technology (Shanghai, China), and transfected into cells by Lipofectamine 3000 (L3000015, Invitrogen, USA) reagent. The sequence of the miRNA mimics used are as follows:

mmu-miR-151-3p: 5′-CUAGACUGAGGCUCCUUGAGG-3′, 5′-CCUCAAGGAGCCUCAGUCUAG-3′.
mmu-miR-221-3p: 5′-AGCUACAUUGUCUGCUGGGUUUC-3′, 5′-GAAACCCAGCAGACAAUGUAGCU-3′.
mmu-miR-423-3p: 5′-AGCUCGGUCUGAGGCCCCUCAGU-3′, 5′-ACUGAGGGGCCUCAGACCGAGCU-3′.
miRNA negative control: 5′-UCACAACCUCCUAGAAAGAGUUAGA-3′, 5′-UCUACUCUUUCUAGGAGGUUGUGA-3′.

2.20 | Oxygen-glucose deprivation model

We used the oxygen-glucose deprivation (OGD) model as previously described (Yuan et al., 2018). Briefly, OGD model was established in a hermetically sealed chamber containing an anaerobic gas mixture (95% N_2 and 5% CO_2). Neuro-2a cells were exposed to glucose-free DMEM (Meilunbio) with oxygen concentration below 1% for 10 h. Then cells were removed from the chamber and the medium was replaced to DMEM supplemented with 10% FBS for 12 h. Neuro-2a cultured in proliferation medium without OGD were used as normal control. As for miRNA mimics transfection, cells were first transfected with mimics for 24 h and then exposed to OGD for 10 h. Cell viability was evaluated via CCK-8 assay. Cells were harvested for Western blot analysis.

2.21 | Image acquirement

Quantitative analysis of the acquired images was performed using both LAS AF Lite (for quantification of cell numbers), ImageJ software (for quantification of fluorescence intensity), and Imaris software (for 3D rendering construction of analyzed cells). Images of four perifocal areas surrounding the lesion core in the ipsilateral hemisphere were taken under a confocal microscope. For EVs uptake and co-localization detection, 40× and 200× images were taken, z-stack = 10, 2.5 μm per section, and the 3D view images were reconstructed in Imaris (9.0.3 Bitplane). The percent number of phagocytic cells was assessed by ImageJ software and DIANA plugin as previously described (Gilles et al., 2017; Shi et al., 2021).

2.22 | Data analysis and statistics

All statistical tests were run in Prism 9.0 (Graphpad). All values are presented as mean ± SD. The number of brain sections, animals used (*n*), and statistical methods were indicated in the figure legends. Statistical analyses were performed one-way ANOVA followed by Tukey's multiple comparisons test, two-way ANOVA followed by Tukey's or Sidak's multiple comparisons, or unpaired Student's *t*-test. Two-tailed $p < 0.05$ were considered statistically significant.

3 | RESULTS

3.1 | Preparation and characterization of ^{125}I/SPIO-PDA@DiR-EVs

BV2 microglia were first polarized to M2 phenotype by treating with 20 ng/mL IL-4 for 48 h, which significantly upregulated M2 phenotype markers ARG and CD206 while did not alter the expression of M1 marker IL-1 and TNF-α (Figure S1A,B). EVs were then isolated from untreated (M0-EVs) and IL-4-treated BV2 cell supernatant (M2-EVs) by ultracentrifugation. Biological TEM images displayed a typical cup-shaped membrane vesicle morphology, with an approximate diameter ranging from 100 to 130 nm (Figure 2a). Nanoparticle tracking analyzer (NTA) confirmed that the hydrated diameter of the EVs was around 130 nm (Figure 2b). To normalize and assess the yield of EVs, we quantified that the protein content of M2-EVs from 300 mL medium was about 2.0 μg/mL using BCA assay, containing roughly 2.0×10^9 particles/mL, as measured by NTA. Western blot results showed that M2-EVs expressed typical EVs markers CD63 and TSG101 (Figure 2c), which meet the minimum standards as outlined in the latest MISEV 2023 guidelines for EV research (Welsh et al., 2024).

To functionalize the surface of EVs with dopamine (PDA), PDA was first oxidized into 5,6-dihydroxyindole (DHI) or catechol-to-catechol coupling, forming a covalent backbone (PDA@EVs), then the DHI groups of covalent backbone coordinated with Fe^{3+} ions of SPIO (SPIO-PDA@EVs). And the indoline groups can also bind to radioactive ^{125}I via an irreversible neighbouring covalent bond. Compared to naïve EVs, PDA@EVs exhibited a similar diameter, dispersity and size distribution (Figure 2a,b). PDA@EVs also expressed CD63 and TSG101, with similar total protein expressions compared to non-coated EVs (Figure 2c,d). Co-expressions of surface EV markers before and after PDA engineering were measured by probing captured $CD81^+$ EVs and $CD9^+$ EVs by Exoview. The data showed that no different expression of EV surface markers including CD63, CD81 and CD9 between EVs and PDA@EVs (Figure 2e).

To test the effects of PDA-labelled EVs on stroke, PDA@EVs or EVs were added to N2a neural cells subjected to OGD. We found that PDA@EVs notably decreased the number of $TUNEL^+$ and Fluoro-Jade C^+ N2a cells after OGD, suggesting PDA could exert neuroprotective effect (Figure S2A–E). For in vivo study, we established a tMCAO mouse model and administered 100 μg of both EVs and PDA@EVs via i.a. injection at 2 h post-stroke. Our findings demonstrated that PDA-modified EVs significantly reduced the number of apoptotic neurons and degenerative neurons at 3 days after stroke, as well as reduced infarct volume (Figure S3A–G), suggesting their neuroprotective effects in stroke.

Next, to visualize the spatial distribution of EVs in the ischemic brain by MRI, amino-functionalized SPIO particles were labelled on the surface of PDA@EVs through Schiff bases reaction. As revealed by the material-type field STEM, PDA@EVs were coated with multiple SPIO particles, each with a diameter of around 10 nm (Figure 2f). The loading efficiency of SPIO on PDA@EVs was 60.03% ± 4.42% after incubation for 48 h in FBS, as measured by an ICP-OES (Table S1). The T2 relaxation time of PDA@EVs, SPIO-PDA@EVs and pure SPIOs were 2698.0 ± 178.5 ms, 177.8 ± 23.5 ms and 25.38 ± 4.17 ms, respectively, measured by 1.41 T NMR analyzer at 37°C. The zeta potential of EVs mildly increased from −17.87 ± 1.16 mV to −15.67 ± 1.16 mV after PDA coating and further increased to −15.63 ± 0.95 mV after SPIO labelling (Figure 2g). Compared with naïve EVs (116.0 ± 5.6 nm) and PDA@EVs (119.3 ± 14.3 nm), there was no significant difference in the hydrodynamic diameter after SPIO labelling (128.0 ± 5.6 nm, $p > 0.05$), as measured by DLS (Figure 2h). Both zeta potential and hydrodynamic diameter of EVs, PDA@EVs and SPIO-PDA@EVs remained stable under physiological conditions (Figure 2g,h).

For comprehensive whole-body visualization of EVs through nuclear techniques, we utilized a classical Iodogen-catalyzed method to label EVs, facilitating subsequent SPECT/CT imaging. The labelling efficiency of ^{125}I on PDA@EVs was around 90% (Figure 2i). Radio-thin-layer chromatography (Radio TCL) showed that the radiochemical purity of ^{125}I -PDA@EVs was 91.05 ± 0.60% and remained 85.20 ± 0.79% after 24-h incubation with 10% FBS in DMEM at 37°C (Figure 2j), indicating relatively stable radiolabelling. STEM-energy dispersive spectrometer detector mapping showed that chemical elements Iodine and Fe were aggregated on the surface of individual ^{125}I/SPIO-PDA@EVs (Figure 2k), indicating successful labelling of both ^{125}I and SPIO on the polydopamine layer of EVs. The labelling efficiency of each step was summarized in Table S1.

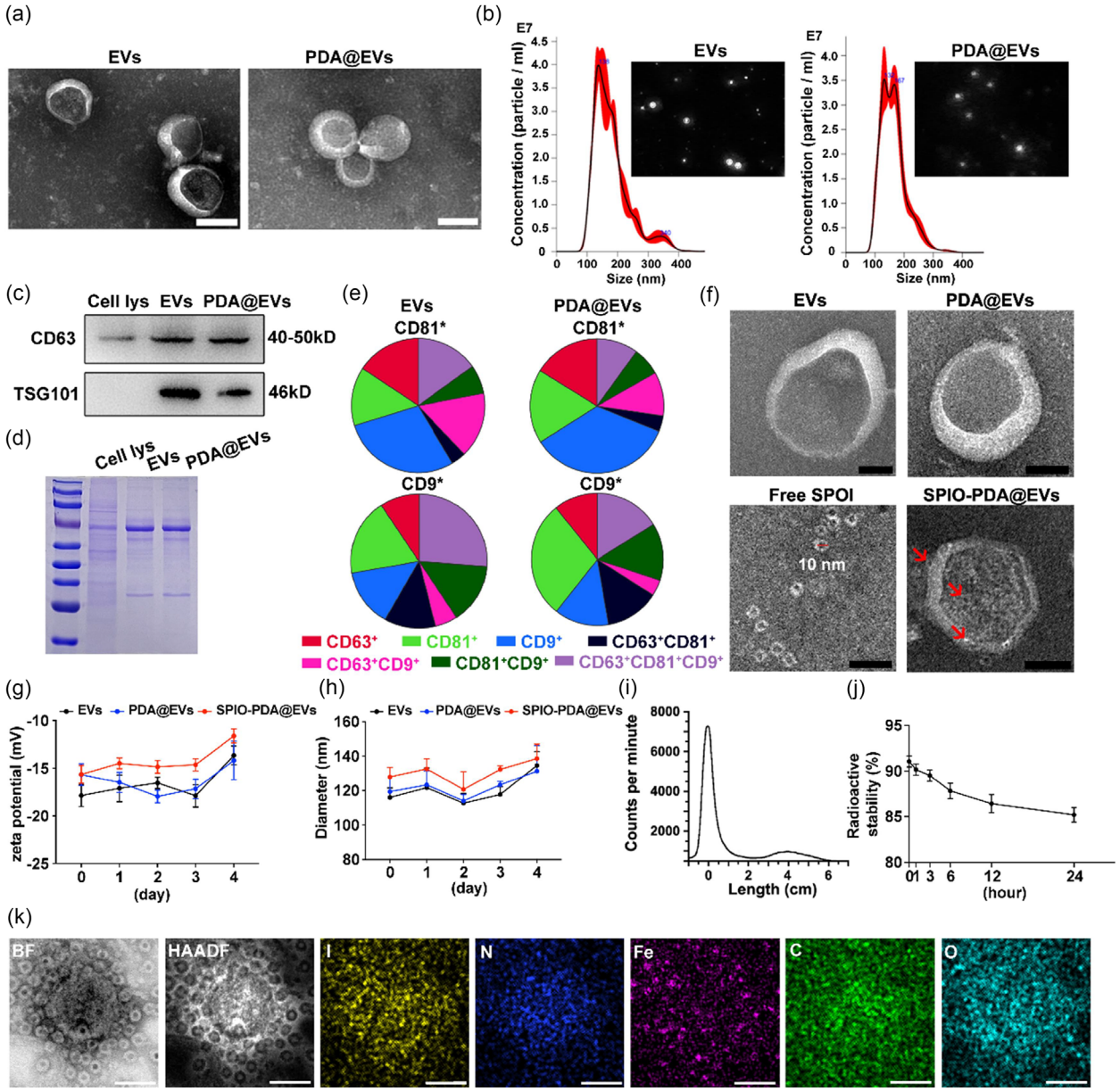

FIGURE 2 Characterization of ^{125}I/SPIO-PDA@EVs. (a) TEM images of EVs and PDA@EVs. Scale bar = 100 nm. (b) Nanoparticle tracking analysis and dynamic snapshots of EVs (left) and PDA@EVs (right). (c) Western blot of EVs markers CD63 (40–50 kD) and TSG101 (46 kD) in M2 BV2 cell lysate, EVs and PDA@EVs. (d) Coomassie brilliant blue staining showed protein bands of M2 BV2 cell lysate, EVs and PDA@EVs. (e) Co-expressions of CD63, CD81 and CD9 in EVs captured by anti-CD81 and anti-CD9 antibodies. (f) STEM images of EVs, PDA@EVs and SPIO-PDA@EVs. Red arrows indicated SPIO. Scale bar = 100 nm. The zeta potential (g) and hydrodynamic diameter (h) of EVs, PDA@EVs and SPIO-PDA@EVs in 10% FBS at different time points. The labelling efficiency of ^{125}I on PDA (i) and radioactive stability of ^{125}I-PDA@EVs (j) in 10% FBS (37°C) at different time points were measured by a radio-thin-layer chromatography. (k) EDS mapping images of distinct compounds of chemical elements for individual ^{125}I/SPIO-PDA@EVs: I, N, Fe, C and O. Scale bar = 50 nm. All data are presented as mean ± SD. The experiment was repeated three times independently. BF, bright field; C, carbon; EDS, energy dispersive spectrometer detector; EV, extracellular vesicle; Fe, ferrum; FBS, foetal bovine serum; HAADF, high-angle annular dark field; I, iodine; N, nitrogen; O, oxygen; PDA, polydopamine; STEM, scanning transmission electron microscope; TEM, transmission electron microscope.

3.2 | RVG29 peptide modification increased neuronal uptake of EVs in vitro

To improve the neuronal uptake of EVs, we conjugated a 29-amino-acid peptide derived from rabies virus glycoprotein (RVG29) to PDA (RVG-PDA@EVs). STEM imaging revealed that the morphology and size of EVs were not altered after RVG29 modification (Figure 3a). The diameter of the RVG-PDA@EVs was 126.0 ± 4.6 nm, and the zeta potential was −15.25 ± 0.51 mV, which was comparable to that of PDA@EVs (130.7 ± 4.7 nm, $p > 0.05$; −15.94 ± 0.85 mV, $p > 0.05$; Figure 3b–c).

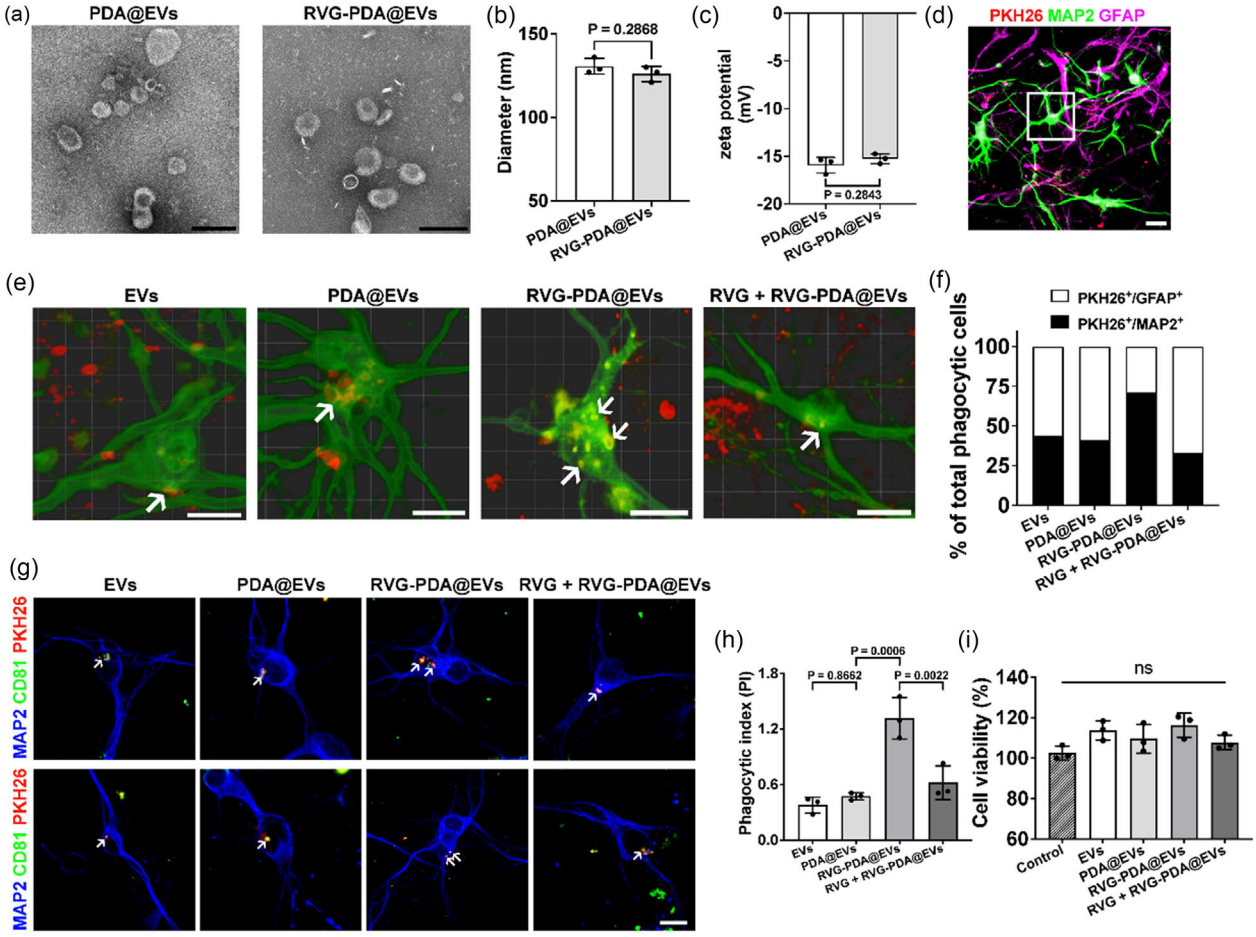

FIGURE 3 RVG29 modification increased neuronal uptake of EVs in vitro. (a) STEM images of PDA@EVs and RVG-PDA@EVs. Scale bar = 100 nm. (b-c) DLS and Zeta potential of PDA@EVs and RVG-PDA@EVs. (d–e) Confocal images showed primary neurons (Green) colocalized with PKH26 labelled naïve EVs, PDA@EVs, RVG-PDA@EVs and RVG-PDA@EVs plus free RVG peptide. White arrows indicated the engulfed EVs. Scale bar = 50 μm. (f) Quantification data showed the percentage of $PKH26^+/GFAP^+$ cells and $PKH26^+/MAP2^+$ cells in total phagocytic cells from different groups. (g) Confocal images showed primary neurons (blue), CD81 (green) and CD9 (green) colocalized with PKH26 labelled (red) naïve EVs, PDA@EVs, RVG-PDA@EVs and RVG-PDA@EVs plus free RVG peptide in vitro. White arrows indicated the engulfed EVs. Scale bar = 10 μm. (h) Quantification showed neuronal phagocytic index from different groups. (i) Cell viability of neurons and glial cells treated with EVs, PDA@EVs, RVG-PDA@EVs and RVG-PDA@EVs plus free RVG peptide for 6 h. The experiment was repeated three times independently. All data are presented as mean ± SD. (b, c) Unpaired Student's *t*-test, two-tailed. (h, i) One-way ANOVA was followed by Tukey's test. DLS, dynamic light scattering; EV, extracellular vesicle; STEM, scanning transmission electron microscope.

3D-reconstruction of confocal images confirmed that PKH26-labelled EVs were localized in the cytoplasm of $MAP2^+$ neurons (Figure 3d–g). We noticed that there was no difference in neuronal uptake in the PDA@EVs group compared to the naïve EVs group ($p > 0.05$). RVG29 modification increased neuronal targeting of EVs by more than 30% compared to the non-RVG modification group (71.22% vs. 41.02%; Figure 3f), and dramatically enhanced neuronal phagocytosis of EVs, compared to naïve EVs ($p < 0.001$) and PDA@EVs ($p < 0.001$; Figure 3h). In addition, the presence of competing free RVG29 peptides (RVG+RVG-PDA@EVs) reduced the neuronal uptake of RVG-modified EVs ($p < 0.01$) (Figure 3e–h). A control group that undergoes the same steps as the engineered EV preparation process but without the addition of EVs was added. The results showed that no PKH26 dye was observed in the cells (Figure S4). CCK-8 assay was performed to assess whether RVG29 conjugation influenced the viability of neurons, and the results showed that RVG-PDA@EVs treatment did not affect the viability of neurons ($p > 0.05$; Figure 3i).

3.3 | i.a. injection yielded the most EVs accumulation in the brain

To ascertain which injection method could deliver the most EVs to the stroke mice brain, DIR dye labelled EVs were first functionalized with PDA, and then modified with SPIO and ^{125}I (^{125}I/SPIO-PDA@DIR-EVs), which allows us to track EVs with MRI/SPECT/Fluorescent multi-modal imaging. One day after stroke, ^{125}I/SPIO-PDA@DIR-EVs were delivered via i.a., i.v. or

i.n. injection (Figure 4a). The delivery efficacy of ^{125}I/SPIO-PDA@EVs administrated by different routes was detailly visualized and carefully evaluated by SPECT, MRI and fluorescent imaging from multiple scales. Laser speckle imaging and CBF quantification confirmed the success of occlusion and reperfusion of mice during tMCAO (Figure S5A,B). After administration, a 7T MRI and T2-weighted (T2W) sequence was applied to investigate the distribution of EVs in the ischemic brain. As shown by T2 images, brain oedema resulted in a hyperintense signal in the injured hemisphere (Figure S5C–E). Stroke mice that received 100 μg (1.0×10^{11} particles) ^{125}I/SPIO-PDA@DIR-EVs through i.a., i.v. or i.n. injections were imaged by MRI at 0.5 h and 24 h post-injection (Figure S5C–E). We found that more ^{125}I/SPIO-PDA@DIR-EVs accumulated in the stroke mice brain at 0.5 h after i.a. injection, compared with that in i.v. and i.n. injection groups (Figure 4b). Similarly, SPECT/CT imaging (Figure S6A–C) and fluorescent imaging (Figure S7A–C) of stroke mice showed that i.a. injection delivered the most ^{125}I/SPIO-PDA@DIR-EVs to the stroke mice brain (Figure 4c–g). Subsequently, we performed immunostaining to determine the cellular uptake of EVs in the brain with i.a. injection. Three-dimensional reconstructed images showed that EVs were mainly phagocytosed by microglia (Iba-1$^+$) and neurons (MAP2$^+$), rather than endothelial cells (CD31$^+$) and astrocytes (GFAP$^+$) (Figure 4h–j).

3.4 | RVG29 peptide modification promoted brain targeting and neuronal uptake of EVs in the ischemic brain

Based on the above results, we applied i.a. injection of RVG engineered ^{125}I/SPIO-PDA@EVs (RVG/^{125}I/SPIO-PDA@EVs) in our further study as i.a. injection achieved maximal efficiency in delivering EVs to stroke mice brain. To visualize the targeting process, stroke mice treated with RVG/^{125}I/SPIO-PDA@EVs were imaged via MR/SPECT/Fluorescent imaging. MRI images showed that more RVG-modified EVs were present in the infarct area of the ischemic brain at 4.5 h post-injection. Even after 48 h post-injection, there were still RVG-modified EVs localized in the lesioned brain (Figure 5a). In contrast, only minimal signal was detected in the brains of mice that received non RVG-modified EVs at 24 h post-injection. Prussian blue staining of brain sections showed that EVs were explicitly localized to the core and peri-infarct areas, and RVG29 modification significantly increased the accumulation of EVs in the ipsilateral hemisphere ($p < 0.05$; Figure 5b–c). SPECT/CT imaging showed that RVG29 modification remarkably increased EVs accumulation in the ischemic brain as compared to non-RVG-modified group ($p < 0.001$). Interestingly, this effect was notably reversed when treating the free RVG29 before injection of RVG-modified EVs (RVG+ RVG/^{125}I/SPIO-PDA@EVs) ($p < 0.01$; Figure 5d–e). Ex vivo fluorescence further confirmed that RVG29 modification indeed improved brain targeting of EVs (Figure 5f–g), as indicated by the significant increase in fluorescence signal ($p < 0.05$). However, when the RVG receptor in the brain was pre-blocked, the enhanced brain targeting of the RVG-modified EVs was reduced ($p < 0.01$; Figure 5f–g). Our immunostaining results further supported that RVG29 modification increased the neuronal uptake of EVs in the infarct area of the striatum ($p < 0.05$; Figure 5h–j). These results collectively highlight the effectiveness of RVG29 modification in enhancing the targeting and retention of therapeutic EVs in the injured brain.

3.5 | Injection of RVG-modified M2-EVs reduced neuronal apoptosis and promoted neurological function recovery in mice after tMCAO

To investigate the therapeutic effect and determine the optimal therapeutic time window of M2-EVs-based therapy, stroke mice were treated with PBS, EVs and RVG-PDA@EVs via i.a. injection at either 2 or 24 h post-tMCAO. Mice that received EVs at 2 h post-tMCAO showed a significant reduction in the number of Fluoro-Jade B (FJ-B)$^+$ cells and TUNEL$^+$ cells at 3 days after tMCAO, indicating decreased neuronal degeneration and apoptosis ($p < 0.05$, $p < 0.05$; Figure 6a–d). RVG-PDA@EVs treatment further decreased neuronal degeneration and apoptosis compared to PBS and EVs treatment ($p < 0.001$, $p < 0.05$, respectively). Western blot showed that RVG-PDA@EVs treatment but not EVs treatment decreased the expression of cleaved caspase-3 ($p < 0.05$; Figure 6e–f). Furthermore, RVG-PDA@EVs treatment significantly reduced neurological deficits and improved motor function as measured by mNSS and rotarod test ($p < 0.01$, $p < 0.05$; Figure 6g–h). However, injection of RVG-PDA@EVs at 24 h post-tMCAO did not yield significant difference in cell apoptosis among the groups ($p > 0.05$; Figure S8A,B). Additionally, mNSS indicated that neither EVs nor RVG-PDA@EVs treatment attenuated neurological deficits at 3 days post-stroke compared to PBS treatment ($p > 0.05$; Figure S8C). Together, these data indicated that polydopamine-based RVG29 modification enhanced the neuroprotective effect of EVs for ischemic stroke, and early intervention, specifically within 2 h of stroke onset, is crucial for achieving optimal therapeutic outcomes.

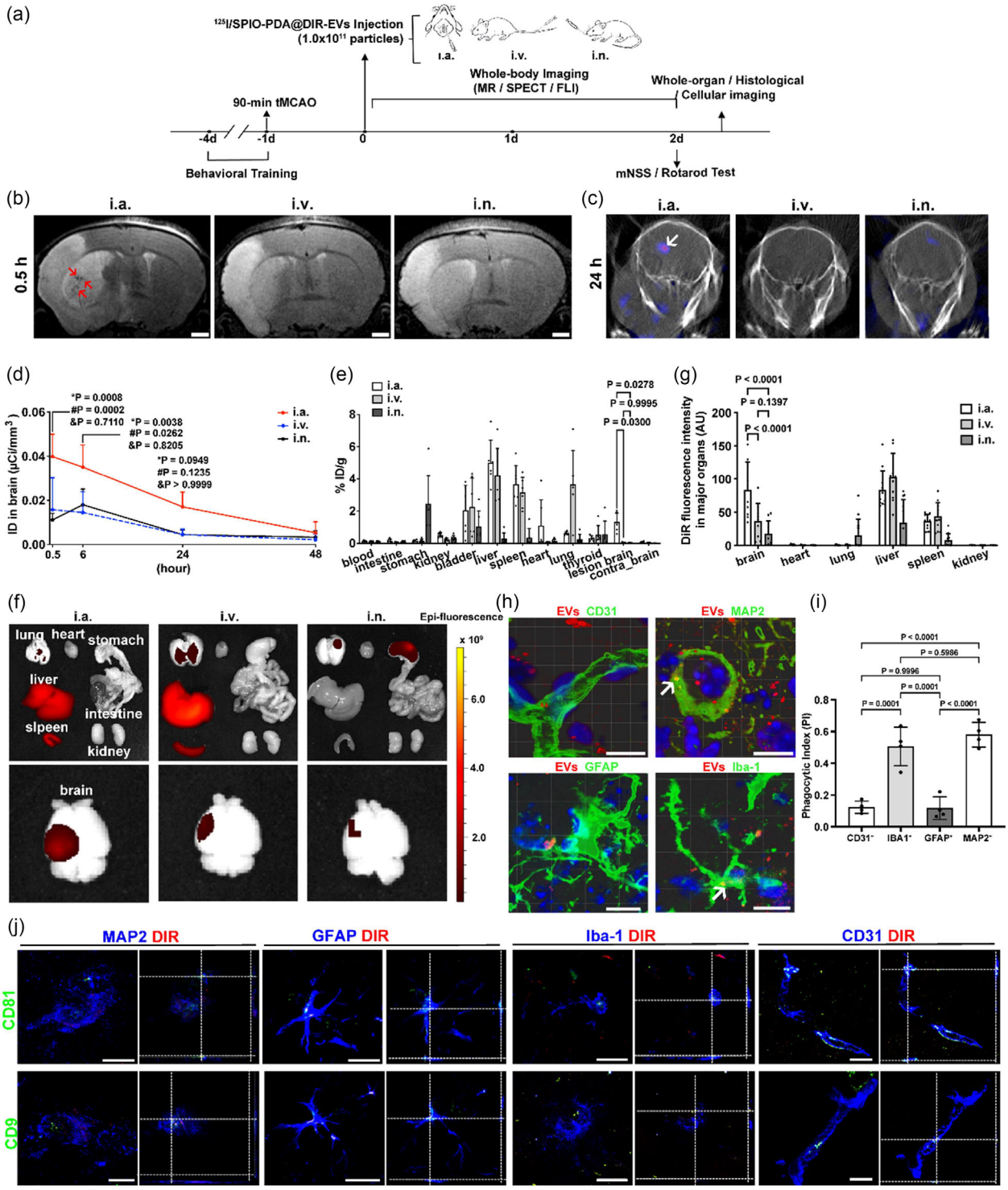

FIGURE 4 MRI/SPECT/Fluorescent imaging showed intra-arterial injection resulted in the most accumulation of EVs in the brain. (a) Schematic process of in vivo experiments. (b) T2-weighted MR images of brain in stroke mouse treated with ^{125}I/SPIO-PDA@DIR-EVs at 0.5 h after tMCAO via i.a., i.v. and i.n. injection. Red arrows indicate the EV signal in the brain. $N = 3$–4 mice per group. Scale bar = 1 mm. (c) SPECT/CT imaging of ^{125}I/SPIO-PDA@DIR-EVs in stroke mice after i.a., i.v. or i.n. injection. (d) The radioactive intensity of ^{125}I/SPIO-PDA@DIR-EVs in stroke mouse brain with various administration routes at different time points. *, i.a. versus i.v.; #, i.a. versus i.n.; &, i.v. versus i.n. $N = 3$–4 mice per group. (e) Bio-distributions of ^{125}I/SPIO-PDA@DIR-EVs in major organs of stroke mice at 48 h after i.a., i.v. or i.n. injections. $N = 6$ mice per group. (f–g) Representative images and quantification showed in vivo distribution of ^{125}I/SPIO-PDA@DIR-EVs in stroke mice at 0.5-, 6-, 24- and 48-h post-i.a., i.v. or i.n. injection. $N = 3$ mice per group. (h) Confocal imaging of brain sections showed ^{125}I/SPIO-PDA@DIR-EVs (Red) co-localized with MAP2$^+$ neurons (green), GFAP$^+$ astrocytes (green), CD31$^+$ endothelial cells (green) and Iba1$^+$ microglia (green). White arrows indicated the engulfed EVs. Scale bar = 10 μm. (i) Bar graph showed the quantification of the phagocytic index of different cell types. $N = 4$ mice per group. (j) Confocal imaging of brain sections showed ^{125}I/SPIO-PDA@DIR-EVs (red), CD81 (green), CD9 (green) co-localized with MAP2$^+$ neurons (blue), GFAP$^+$ astrocytes (blue), Iba1$^+$ microglia (blue) and CD31$^+$ endothelial cells (blue). Scale bar = 10 μm. All data are presented as mean ± SD. EV, extracellular vesicle; i.a., intra-arterial; i.n.; intra-nasal; i.v.; intravenous; PDA, polydopamine; tMCAO, transient middle cerebral artery occlusion.

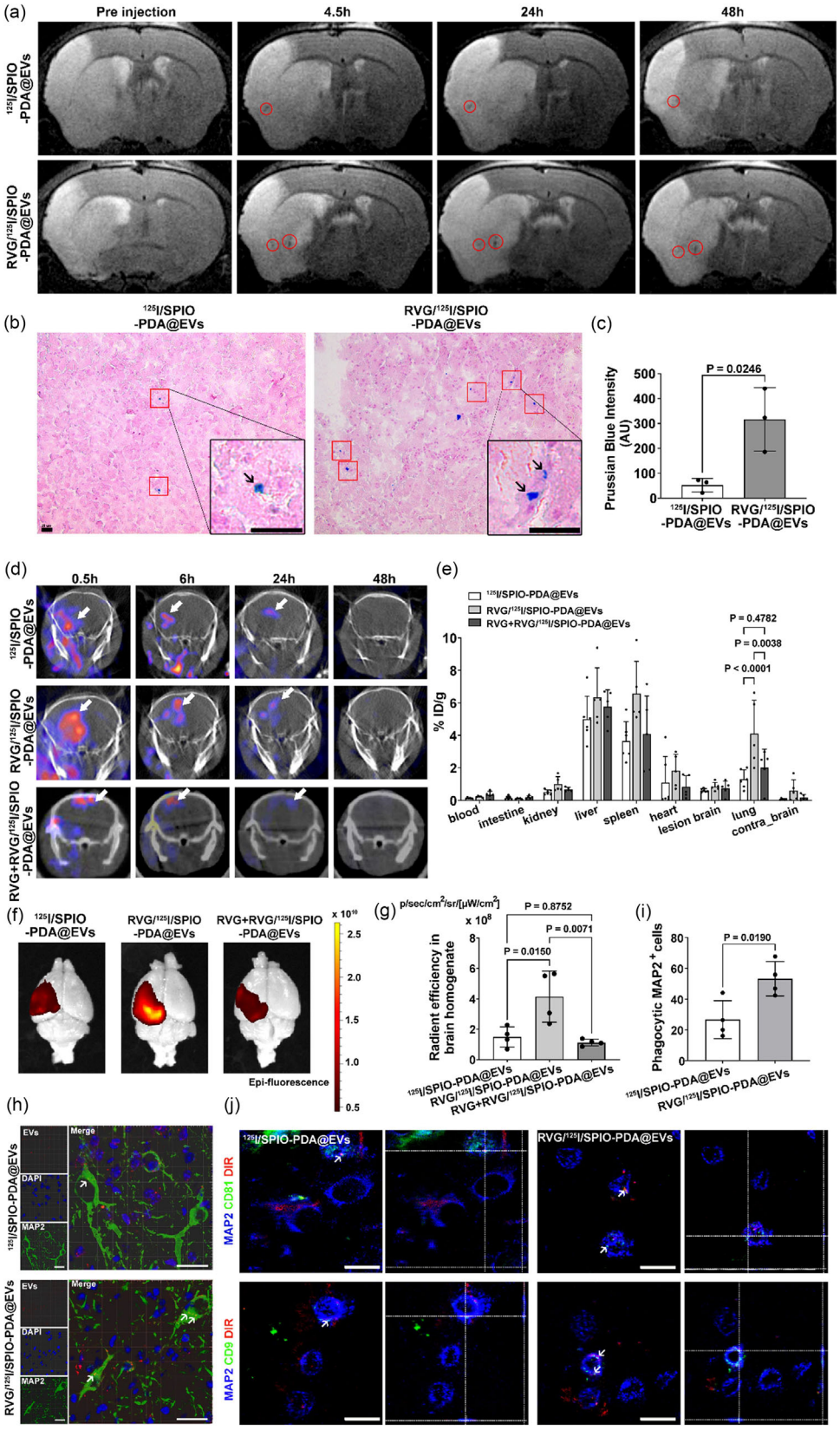

FIGURE 5 RVG29 modification promoted targeted delivery of EVs in the ischemic brain. (a) MR imaging of the brain from stroke mice received ^{125}I/SPIO-PDA@EVs and RVG/^{125}I/SPIO-PDA@EVs before injection and 4.5-, 24- and 48- h post-i.a. injection. Red circles indicated the signal of EVs. $N = 3$ mice per group. (b–c) Prussian blue staining of brain sections after 48 h following injection of RVG/^{125}I/SPIO-PDA@EVs. Black arrows indicated the EVs engulfed by cells. Scale bar = 25 μm. $N = 3$ mice per group. (d–e) SPECT/CT imaging and biodistribution of stroke mice received ^{125}I/SPIO-PDA@EVs, RVG/^{125}I/SPIO-PDA@EVs, or RVG+RVG/^{125}I/SPIO-PDA@EVs at 0.5-, 6-, 24- and 48- h post-i.a. injection. White arrows indicated the EVs signals in the brain. $N = 5$–6 mice per group. (f–g) Representative fluorescence images of the brain sections from stroke mice received ^{125}I/SPIO-PDA@EVs,

(Continues)

FIGURE 5 (Continued)
RVG/^{125}I/SPIO-PDA@EVs, or RVG+RVG/^{125}I/SPIO-PDA@EVs at 48 h post-i.a. injection. (h) Confocal imaging showed the co-localization of EVs (Red) with MAP2^{+} neurons (green). DAPI, blue. Scale bar = 20 μm. (i) Quantification of the number of phagocytic neurons per field from the stroke mice receiving EVs or RVG-modified EVs. $N = 3$ mice per group. All data are presented as mean ± SD. (j) Confocal imaging of brain sections showed ^{125}I/SPIO-PDA@DIR-EVs (red), CD81 (green), CD9 (green) co-localized with MAP2^{+} neurons (blue) in ^{125}I/SPIO-PDA@EVs and RVG-^{125}I/SPIO-PDA@EVs groups. White arrows indicated the engulfed EVs. Scale bar = 10 μm. (e) Two-way ANOVA followed by Tukey's test. (c, g, i) Unpaired Student's *t*-test, two-tailed. i.a., intra-arterial; EV, extracellular vesicle; PDA, polydopamine.

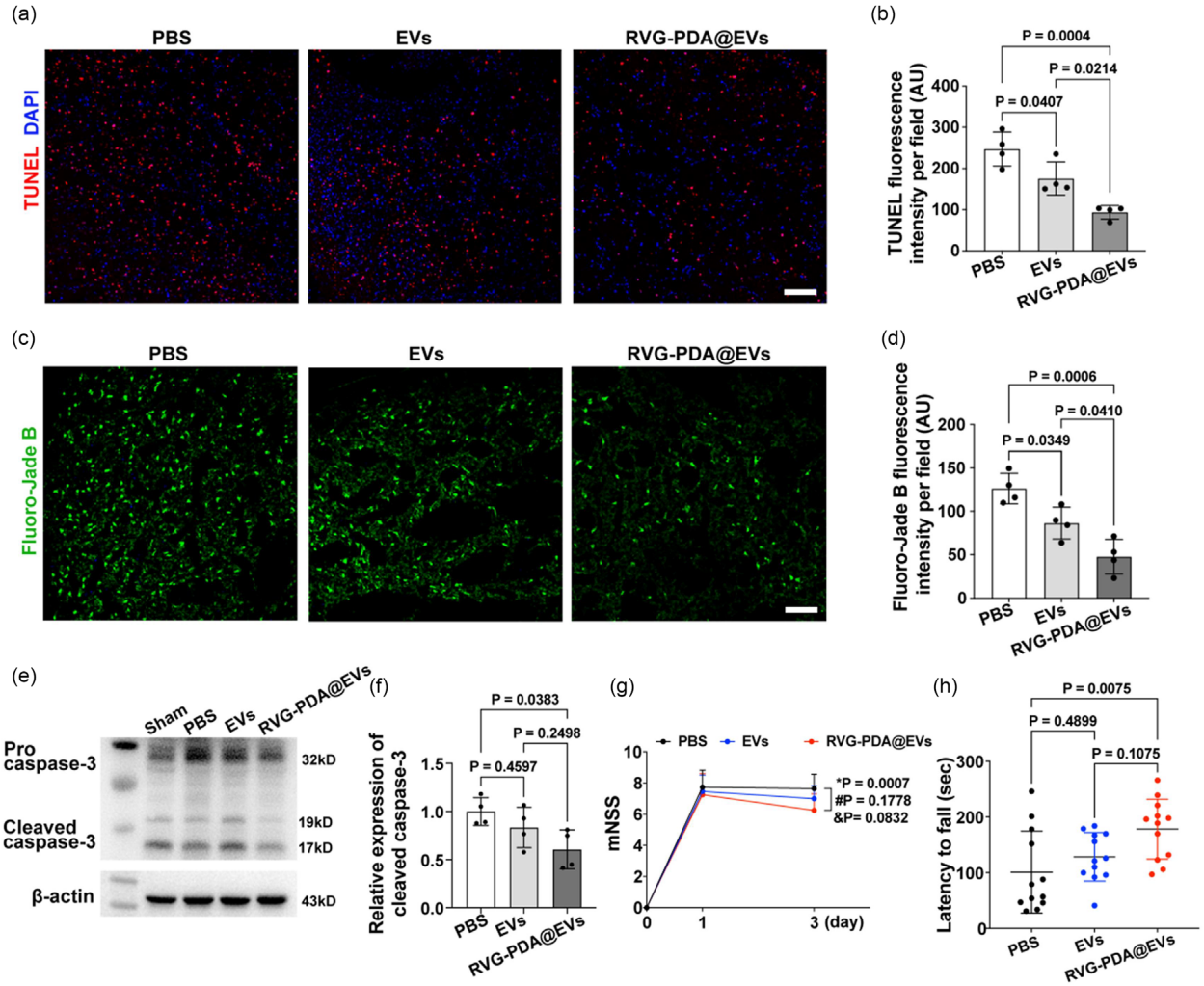

FIGURE 6 RVG-modified M2-EVs further reduced neuronal apoptosis and promoted neurological function recovery in mice after tMCAO. TUNEL staining (a–b) and Fluoro-Jade B staining (c–d) showed neuronal death in stroke mice treated with PBS, EVs or RVG-PDA@EVs. Scale bar = 100 μm in (a) and 50 μm in (c). $N = 4$ mice per group. Western blot (e–f) of Pro-caspase-3 (32 kD), Cleaved caspase-3 (19 and 17 kD) and β-actin (43 kD) expression in stroke mice treated with PBS, EVs and RVG-PDA@EVs. $N = 4$ mice per group. Neurobehavioral tests showed mNSS (g) and rotarod test (h) of mice treated with PBS, EVs and RVG-PDA@EVs at 2 h after tMCAO. *, PBS versus EVs; #, PBS versus RVG-PDA@EVs; &, EVs versus RVG-PDA@EVs. $N = 11$–13 mice per group. All data are presented as mean ± SD. (b, d, f, h) One-way ANOVA was followed by Tukey's test. (g) Two-way ANOVA was followed by Tukey's test. EV, extracellular vesicle; M2-EV, M2 microglia-derived EV; PDA, polydopamine; tMCAO, transient middle cerebral artery occlusion.

3.6 | M2-EVs upregulated anti-apoptosis related miRNAs and ameliorated apoptosis through p38/ERK pathway

To investigate the neuroprotective mechanism mediated by RVG-PDA@EVs, we performed EVs miRNA array (Table S2). Principal component analysis revealed a dispersed sample in the RVG-PDA@EVs group, which was excluded for further analysis to avoid biasing the results (Figure 7a). EVs from M0 microglia (M0-EVs) and EVs from M2 microglia (M2-EVs) exhibited distinct gene expression profiles, while RVG modified M2-EVs (RVG-PDA@EVs) and M2-EVs shared similar gene expressions. Specifically, 35 differentially expressed miRNAs were identified in M2-EVs compared to M0-EVs, among which 21 miRNAs

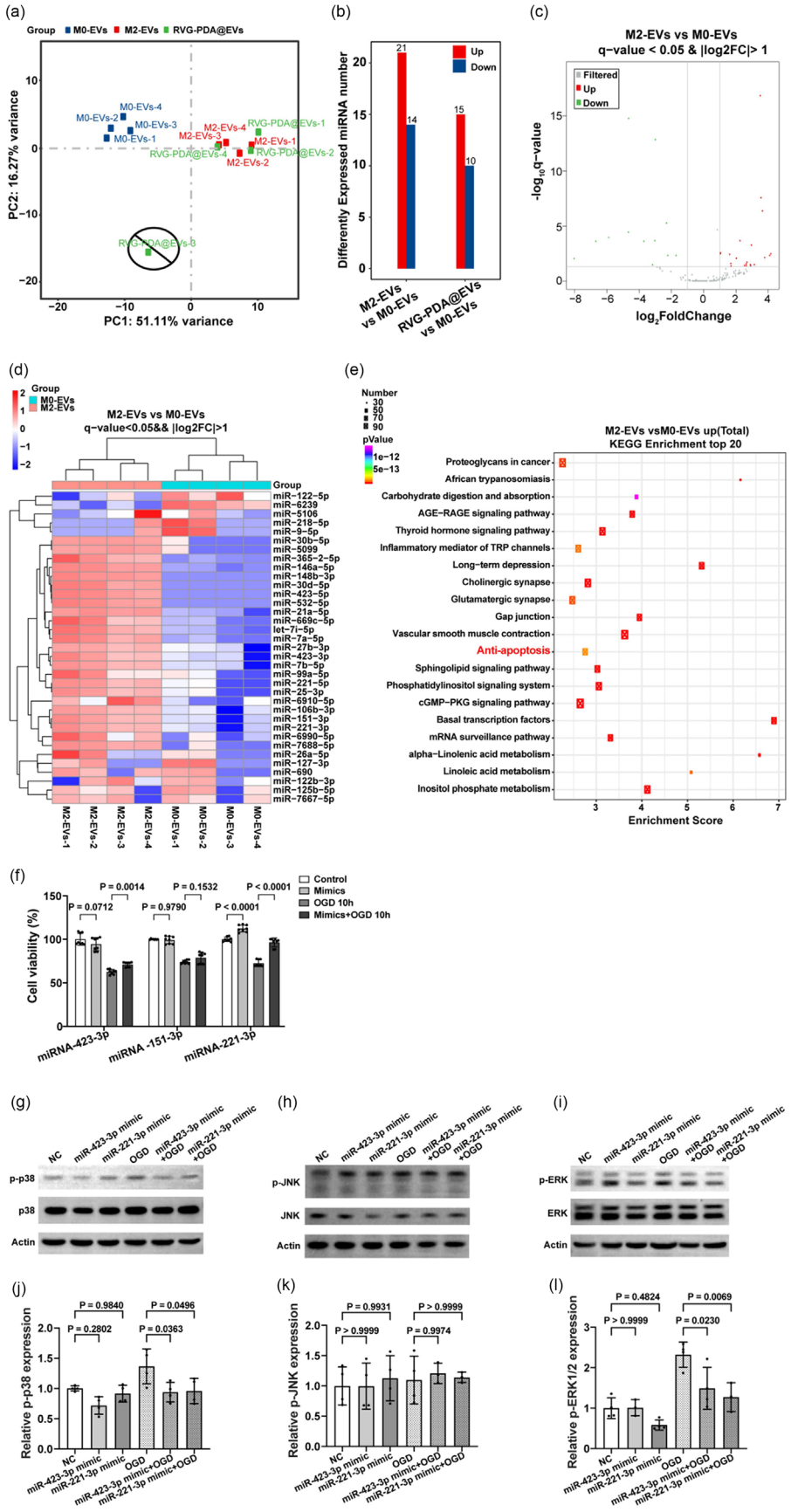

FIGURE 7 M2-EVs upregulated apoptosis-related miRNAs and ameliorated apoptosis through p38/ERK pathway. (a) PC analysis of miRNA array data from EVs from M0 microglia (M0-EVs), M2 microglia (M2-EVs) and RVG modified M2-EVs (RVG-PDA@EVs). (b) The bar graph showed differentially

(Continues)

FIGURE 7 (Continued)
expressed miRNAs in the M2-EVs and M0-EVs. (c-d) Heat map and volcano plots showed top differentially expressed miRNAs between M2 and M0 groups. (e) The dot graph showed the top 20 pathways upregulated in the M2 group versus the M0 group. q value < 0.05, fold change > 2. (f) CCK-8 analysis of Neuro-2a cells treated with miRNA NC or miRNA mimics, under OGD condition, or treated with miRNA mimics prior to OGD. (g–l) Western blot and statistical analysis of p-p38/p38, p-JNK/JNK and p-ERK/ERK expression in Neuro-2a cells under different conditions. The experiment was repeated at least three times independently. One-way ANOVA was followed by Tukey's test. All data are presented as mean ± SD. EV, extracellular vesicle; OGD, oxygen-glucose deprivation; PC, principal component; PDA, polydopamine; M2-EV, M2 microglia-derived EV; NC, negative control.

were upregulated, and 14 miRNAs were downregulated ($q < 0.05$, fold change (FC) > 2; Figure 7b). The heatmap and volcano plots of these differentially expressed miRNA were depicted in Figure 7c,d. Most of the upregulated miRNAs were also within the range of top 20 relatively abundant genes in M2-EVs, including miR-21a-5p, miR-151-3p, miR-7b-5p and so forth. Importantly, no differentially expressed miRNAs were found between M2-EVs and RVG-PDA@EVs ($q < 0.05$, FC > 2), indicating that polydopamine based RVG labelling strategy did not alter the miRNAs content of EVs. KEGG analysis revealed that metabolic signalling, synapse, vascular function and anti-apoptosis-related pathways were enriched in M2-EVs (Figure 7e, Table S3). These findings suggested that M2-EVs may exert neuroprotective effects in stroke mice via those anti-apoptosis-related miRNAs.

Among these top-upregulated miRNAs in M2-EVs, three miRNAs have been validated by qPCR in our previous work, specifically miR-151-3p, miR-221-3p, miR-423-3p, all of which were enriched in M2-EVs compared to M0-EVs (Li et al., 2022). CCK-8 assay showed that pre-treatment with miR-423-3p or miR-221-3p mimics significantly improved neuronal viability by approximately 14% ($p < 0.001$) and 33% ($p < 0.001$), respectively, whereas miR-151-3p mimics treatment showed no significant difference ($p > 0.05$; Figure 7f). Western blot results revealed a significant decrease in p-p38 ($p < 0.05$, $p < 0.05$), and p-ERK1/2 ($p < 0.05$, $p < 0.01$), but not in p-JNK ($p > 0.05$, $p > 0.05$), in Neuro-2a cells pre-treated with miR-221-3p or miR-423-3p mimics, respectively (Figure 7g–l). Collectively, these results suggest that miR-221-3p and miR-423-3p contributed to the anti-apoptotic effects of M2-EVs by modulating the p38/ERK signalling pathways.

4 | DISCUSSION

EVs-based therapy holds great promise for stroke treatment. However, inefficient targeted delivery of EVs hinders its clinical translation. To address this challenge, we developed a PDA-based platform which allows easily simultaneous labelling neuronal targeting peptide and multi-mode imaging tracers on EVs. To determine the most appropriate administration routes for targeted delivery of EVs, we tracked the engineered EVs in vivo with SPECT, MRI and fluorescent imaging from multiple scales, and demonstrated that i.a. injection achieved the maximal efficient delivery of engineered EVs to the stroke mice brain, compared with i.v. and intranasal injection. Notably, RVG29 modification showed excellent neuronal targeting capability, enhanced therapeutic efficacy by reducing neuronal apoptosis post-stroke. Furthermore, through EVs miRNA array, we discovered that M2-EVs may exert neuroprotective effects by upregulating miR-221-3p and miR-423-3p, which are involved in modulating the p38/ERK pathway.

Developing strategies that can simultaneously targeted deliver EVs and monitor the targeting process in real-time is crucial for disease treatment. In this context, we designed a PDA-based strategy to simultaneously label EVs with neuronal targeting peptide RVG29, as well as SPIOs, radioactive ^{125}I and fluorescent dyes as functional units for enhancing the delivery efficiency and quantitatively track the labelled EVs in vivo. PDA, a dopamine-derived synthetic eumelanin polymer, is widely used for surface coating due to its good biocompatibility, stability and ROS clearance in inflammatory conditions. These properties were confirmed by our results, which demonstrated that PDA coating did not significantly alter the size, morphology and surface biological makers of EVs. We observed several aggregated EV particles, as shown by TEM in addition, imaging results showed significant accumulation of EVs in the injured brain and increased uptake by neurons, suggesting PDA coating did not affect the recognition process. Our findings also indicated that PDA coating effectively preserves the therapeutic potential of the EVs, as demonstrated by promising therapeutic outcomes. Besides, PDA has been demonstrated to act as smart ROS scavengers in oxidative stress (Xu et al., 2023); thus, the PDA layer could serve as a protective shell on EVs, helping them withstand oxidative stress, inflammation and mechanical injury common in ischemic stroke (Kuriakose & Xiao, 2020), thereby maintaining their structural stability.

Non-invasive in vivo visualizing EVs is still particularly challenging due to their small size (Veziroglu & Mias, 2020). While several noninvasive imaging modalities have been developed and utilized for EVs tracking and visualization, each has its pros and cons (Wu & Shu, 2018). Multimodal imaging can overcome their respective limitations and achieve more accurate information on quantitative monitoring of transplanted EVs at levels ranging from whole-body to single-cellular and even molecular, and allows us to quantitatively track the labelled EVs in vivo with high spatial resolution, high sensitivity and anatomical localization. Our study applied SPIO for MR imaging because it was clinically approved and showed better phase contrast in the stroke brain than gadolinium-based agents (Wang, 2011). However, given the relatively low sensitivity of MRI, SPECT imaging was further performed due to its high-sensitivity, low cost and widely establishment. Here we chose ^{125}I due to its relatively long half-life and

easy to be labelled compared with other radioisotopes such as ^{111}In (Ailuno et al., 2020), and ^{18}F (Chen, Lu et al., 2021), enabling long-term tracking of labelled EVs.

In our study, EVs signals obtained from SPECT were considerably stronger than MRI, and could be detected up to 24 h after injection, while MR imaging could only detect EVs signals up to 6 h after injection, underscoring the higher sensitivity of SPECT imaging(Nobuta et al., 2011). We compared the signals among i.v., i.a. and intranasal injections and found that i.a. injection resulted in the most robust and durable signals in the brain. Conversely, i.v. injections predominantly resulted in EVs accumulation in the liver, and intranasal injection led to minimal signals in the brain, possibly due to impeded EVs migration by nasal cilia. However, Betzer et al. reported that intranasal administration of GNP-labelled EVs led to a higher number of EVs in the brain than i.v. administration (Betzer et al., 2017), which was inconsistent with our study. This could be attributed to different modifications on EVs surface. It is possible that hydrophilic PDA coating may reduce the absorbance by nasal epithelium and improve the adhesion to nasal cilia of EVs. It is worth noting that some of the EVs might reach the oesophagus due to the proximity of the nasal and oral cavities in mice. To mitigate this, here we used a 10 μL pipette tip to slowly administer EVs into the nasal cavity to ensure complete absorption; and we've ensured good dispersity of our EVs, minimizing the potential for aggregation. Utilizing a spray application might improve the absorption of EVs into nasal mucosa, but the potential contamination of the fur or skin of the mice with contrast agents labelled EVs, would inevitably introduce unwanted background signal during imaging. Thus, strategies to enhance the efficacy of nasal administration should be explored in future studies. By SPECT/CT imaging, we found that minimal signal could be detected at 24 h after i.v. and intranasal injection, while a number of EVs were still present in the brain after i.a. injection. This suggested that i.a. injection surpasses other methods of efficiently delivering EVs to the brain.

Our study holds significant translational potential and provides an in-depth understanding of EVs biodistribution and behavior in vivo, which is critical for designing EVs-based therapeutic protocols, including determining the optimal dose, injection frequency, and the most effective administration route for clinical application. By enhancing brain-specific targeting, we further improved the therapeutic efficacy of EVs for stroke. However, translating this from bench to bedside does face certain challenges. One key challenge is understanding the heterogeneity of EVs derived from different cell sources and their corresponding cargos. Since the therapeutic potential of EVs largely depends on their content, the variation in EV content from different cell sources could lead to inconsistent therapeutic outcomes. Another challenge lies in the reproducible, cost-effective large-scale production of brain-targeted EVs. Moreover, the effectiveness of our approach also needs to be evaluated across a broad spectrum of neurological disorders to fully understand its therapeutic potential and limitations.

In this study, we sought to delineate the role of apoptosis-related miRNAs enriched in M2-EVs in promoting neuroprotection following ischemic stroke. Our miRNA sequencing data revealed a distinct miRNA profile in M2-EVs compared to M0-EVs, with several miRNAs involved in anti-apoptotic pathways being upregulated. The enrichment of miR-423-3p, miR-7688-5p, miR-106b-3p, miR-532-5p, miR-151-3p, miR-146a-5p, miR-221-3p and so forth, in M2-EVs suggests that these miRNAs may act in concert to modulate apoptosis-related pathways, ultimately contributing to neuronal survival. Our findings are consistent with previous studies that demonstrated the neuroprotective roles of miR-423-3p and miR-532-5p in ameliorating hypoxia-induced cell apoptosis (Luo et al., 2019; Ma et al., 2018). For instance, MiRNA-423-3p, which shows increased level in cardiac fibroblasts-derived EVs and could regulate Ras-related protein Rap-2c (RAP2C) expression in H9C2 cells; knockdown of RAP2C led to enhanced cell viability and decreased apoptosis under hypoxia-reoxygenation injury (Luo et al., 2019). Similarly, miR-532-5p has been shown to mitigate hypoxia-induced apoptosis in H9C2 cells by directly targeting PDCD4 (Ma et al., 2018). Additionally, microRNA-151-3p, abundant in microglia-derived EVs, contributes to mediating neuroprotective effect in spinal cord injury repair via p53/p21/CDK1 pathways (Li, Qin et al., 2021). Moreover, a recent study showed that treatment with miR-146a-5p mimetics downregulated pro-apoptotic signalling pathways in the visceral adipose tissue of long-living Ames dwarf mice (Nunes et al., 2022). MiR-221-3p and miR-30b-5p also have been identified as crucial players in suppressing cell apoptosis and anti-inflammation (Wu et al., 2020; Yang et al., 2021). The synergistic action of these miRNAs highlights the complexity of the molecular mechanisms involved in ischemic stroke and the potential therapeutic benefits of M2-EVs. In our study, we identified two miRNAs upregulated in M2-EVs, miR-221-3p and miR-423-3p, which could potentially exert neuroprotective effects via the p38/ERK apoptotic pathways. However, further research is necessary to fully comprehend the specific targets these miRNAs directly regulate in the context of ischemic stroke.

There are several novelties of our study. First, we developed a simple and efficient PDA-based platform for simultaneously labelling EVs with targeting peptides and various imaging probes without affecting EVs function, which allows targeted delivery of M2-EVs to stroke mice brain and enabled the dynamic visualization of the targeting process from whole-body to cellular levels. Additionally, such PDA modification can exert neuroprotective effect and enhance the therapeutic effects of EVs for stroke. The PDA-based platform achieved multiple effects in a single step. Second, using this platform, multifunctional EVs were prepared, and multimodal imaging (including MRI, SPECT/CT and fluorescence imaging) was systematically performed, revealing distinct EV distribution patterns following different injection methods post-stroke. Results indicated that arterial delivery leads to higher EV accumulation in the brain, providing a theoretical basis for future clinical translation. Third, our study provided a comprehensive analysis of the therapeutic effects of M2-EVs on stroke, demonstrating that M2-EVs exert neuroprotective effects via miR-221-3p and miR-423-3p.

In conclusion, polydopamine-based RVG and multi-mode tracers co-labelling strategy effectively equips EVs with dual ischemic brain-targeting and multiscale visualization capabilities, substantially enhancing their therapeutic efficacy. Our study provided a promising therapeutic agent, and an efficient, safe EVs delivery platform for stroke therapy, which will contribute to the optimization of clinical strategies for EV therapy in the near future.

AUTHOR CONTRIBUTIONS

Xiaojing Shi: Conceptualization(equal); Data curation(equal); Formal analysis(equal); Investigation(equal); Methodology(equal); Writing—original draft(equal). **Lu Zhang**: Conceptualization(equal); Data curation(equal); Formal analysis(equal); Investigation(equal); Methodology(equal); Writing—original draft(equal). **Shengju Wu**: Data curation(equal); Investigation(equal); Methodology(equal); Writing—review & editing(equal). **Chunfu Zhang**: Conceptualization(supporting); Investigation(supporting); Methodology(supporting). **Muyassar Mamtilahun**: Data curation(supporting); Methodology(supporting). **Yongfang Li**: Data curation(supporting); Investigation(supporting); Methodology(supporting). **Zhijun Zhang**: Funding acquisition(supporting); Methodology(supporting); Project administration(supporting). **Changjing Zuo**: Investigation(supporting); Project administration(supporting). **Fengzhen Cui**: Data curation(supporting); Methodology(supporting) Wanlu Li: Funding acquisition(supporting); Project administration(supporting). **Guo-Yuan Yang**: Project administration(supporting). **Yaohui Tang**: Funding acquisition(supporting); Project administration(equal); Writing-original draft(equal).

ACKNOWLEDGEMENTS

We would like to thank the Department of Nuclear Medicine, Fudan University Shanghai Cancer Center (Shanghai, China) for providing SPECT/CT imaging and MR imaging, Dr. Jian-Ping Zhang, Dr. Cong Li and Dr. Jian Chen for their assistance with animal imaging, and Dr. Qidong Zu and Biao Li for their support with EVs miRNA sequence analysis. This study was supported by grants from the National Natural Science Foundation of China, 82371307 (Y.T.), 81901804 (L.Z.), 82172529 (J.W.), 82472590 (J.W.), 82271320 (Z.Z.), the National Key R&D Program of China, #2022YFA1603600 (Z.Z.), Young Leading Scientists Cultivation Plan supported by Shanghai Municipal Education Commission, ZXWH1082101 (Y.T.), the Fundamental Research Funds for the Central Universities, YG2023ZD02 (Y.T.), SUITM-202306 (Y.T.), Shanghai Sailing Program, 23YF1420700 (W.L.).

CONFLICT OF INTEREST STATEMENT

The authors declare no competing interests.

DATA AVAILABILITY STATEMENT

Raw data are provided in the supporting information. The raw sequence data of miRNA-seq reported in this paper have been deposited in the Genome Sequence Archive (Genomics, Proteomics & Bioinformatics 2021) in National Genomics Data Center (Nucleic Acids Res 2022), China National Center for Bioinformation/Beijing Institute of Genomics, Chinese Academy of Sciences (GSA: CRA010443) that are publicly accessible at https://ngdc.cncb.ac.cn/gsa (Chen, Chen et al., 2021; Members & Partners, 2022). Uncut Western blot images are shown in Figure S9.

ORCID

Yaohui Tang https://orcid.org/0000-0002-9603-2650

REFERENCES

Ailuno, G., Baldassari, S., Lai, F., Florio, T., & Caviglioli, G. (2020). Exosomes and extracellular vesicles as emerging theranostic platforms in cancer research. *Cells*, *9*, 2569.

Banks, W. A., Sharma, P., Bullock, K. M., Hansen, K. M., Ludwig, N., & Whiteside, T. L. (2020). Transport of extracellular vesicles across the blood-brain barrier: Brain pharmacokinetics and effects of inflammation. *International Journal of Molecular Sciences*, *21*, 4407.

Betzer, O., Perets, N., Angel, A., Motiei, M., Sadan, T., Yadid, G., Offen, D., & Popovtzer, R. (2017). In vivo neuroimaging of exosomes using gold nanoparticles. *ACS Nano*, *11*, 10883–10893.

Chen, T., Chen, X., Zhang, S., Zhu, J., Tang, B., Wang, A., Dong, L., Zhang, Z., Yu, C., Sun, Y., Chi, L., Chen, H., Zhai, S., Sun, Y., Lan, L., Zhang, X., Xiao, J., Bao, Y., Wang, Y., … Zhao, W. (2021). The genome sequence archive family: Toward explosive data growth and diverse data types. *Genomics, Proteomics & Bioinformatics*, *19*, 578–583.

Chen, Y. A., Lu, C. H., Ke, C. C., Chiu, S. J., Jeng, F. S., Chang, C. W., Yang, B. H., & Liu, R. S. (2021). Mesenchymal stem cell-derived exosomes ameliorate Alzheimer's disease pathology and improve cognitive deficits. *Biomedicines*, *9*, 594.

Colvett, I., Saternos, H., Coughlan, C., Vielle, A., & Ledreux, A. (2023). Extracellular vesicles from the CNS play pivotal roles in neuroprotection and neurodegeneration: Lessons from in vitro experiments. *Extracellular Vesicles and Circulating Nucleic Acids*, *4*, 72–89.

Enright, A. J., John, B., Gaul, U., Tuschl, T., Sander, C., & Marks, D. S. (2003). MicroRNA targets in *Drosophila*. *Genome biology*, *5*, R1.

Friedlander, M. R., Mackowiak, S. D., Li, N., Chen, W., & Rajewsky, N. (2012). miRDeep2 accurately identifies known and hundreds of novel microRNA genes in seven animal clades. *Nucleic Acids Research*, *40*, 37–52.

Gilles, J. F., Dos Santos, M., Boudier, T., Bolte, S., & Heck, N. (2017). DiAna, an ImageJ tool for object-based 3D co-localization and distance analysis. *Methods*, *115*, 55–64.

Gonzalez, M. I., Gonzalez-Arjona, M., Santos-Coquillat, A., Vaquero, J., Vazquez-Ogando, E., de Molina, A., Peinado, H., Desco, M., & Salinas, B. (2021). Covalently labeled fluorescent exosomes for in vitro and in vivo applications. *Biomedicines*, *9*, 81.

Griffiths-Jones, S., Bateman, A., Marshall, M., Khanna, A., & Eddy, S. R. (2003). Rfam: An RNA family database. *Nucleic Acids Research*, *31*, 439–441.

Griffiths-Jones, S., Saini, H. K., van Dongen, S., & Enright, A. J. (2008). miRBase: Tools for microRNA genomics. *Nucleic Acids Research*, *36*, D154–D158.

Guan, P., Fan, L., Zhu, Z., Yang, Q., Kang, X., Li, J., Zhang, Z., Liu, S., Liu, C., Wang, X., Xu, J., Wang, K., & Sun, Y. (2024). M2 microglia-derived exosome-loaded electroconductive hydrogel for enhancing neurological recovery after spinal cord injury. *Journal of Nanobiotechnology*, *22*, 8.

Jang, Y., Kim, H., Yoon, S., Lee, H., Hwang, J., Jung, J., Chang, J. H., Choi, J., & Kim, H. (2021). Exosome-based photoacoustic imaging guided photodynamic and immunotherapy for the treatment of pancreatic cancer. *Journal of Controlled Release*, *330*, 293–304.

Kumar, P., Wu, H., McBride, J. L., Jung, K. E., Kim, M. H., Davidson, B. L., Lee, S. K., Shankar, P., & Manjunath, N. (2007). Transvascular delivery of small interfering RNA to the central nervous system. *Nature*, *448*, 39–43.

Kuriakose, D., & Xiao, Z. (2020). Pathophysiology and treatment of stroke: Present status and future perspectives. *International Journal of Molecular Sciences*, *21*, 7609.

Kwon, E. J., Skalak, M., Lo Bu, R., & Bhatia, S. N. (2016). Neuron-targeted nanoparticle for siRNA delivery to traumatic brain injuries. *ACS Nano*, *10*, 7926–7933.

Lemaster, J. E., Wang, Z., Hariri, A., Chen, F., Hu, Z., Huang, Y., Barback, C. V., Cochran, R., Gianneschi, N. C., & Jokerst, J. V. (2019). Gadolinium doping enhances the photoacoustic signal of synthetic melanin nanoparticles: A dual modality contrast agent for stem cell imaging. *Chemistry of Materials*, *31*, 251–259.

Li, C., Qin, T., Liu, Y., Wen, H., Zhao, J., Luo, Z., Peng, W., Lu, H., Duan, C., Cao, Y., & Hu, J. (2021). Microglia-derived exosomal microRNA-151-3p enhances functional healing after spinal cord injury by attenuating neuronal apoptosis via regulating the p53/p21/CDK1 signaling pathway. *Frontiers in Cell and Developmental Biology*, *9*, 783017.

Li, Y., Liu, Z., Song, Y., Pan, J. J., Jiang, Y., Shi, X., Liu, C., Ma, Y., Luo, L., Mamtilahun, M., Shi, Z., Khan, H., Xie, Q., Wang, Y., Tang, Y., Zhang, Z., & Yang, G. Y. (2022). M2 microglia-derived extracellular vesicles promote white matter repair and functional recovery via miR-23a-5p after cerebral ischemia in mice. *Theranostics*, *12*, 3553–3573.

Li, Z., Song, Y., He, T., Wen, R., Li, Y., Chen, T., Huang, S., Wang, Y., Tang, Y., Shen, F., Tian, H. L., Yang, G. Y., & Zhang, Z. (2021). M2 microglial small extracellular vesicles reduce glial scar formation via the miR-124/STAT3 pathway after ischemic stroke in mice. *Theranostics*, *11*, 1232–1248.

Liu, H., Geng, Z., & Su, J. (2022). Engineered mammalian and bacterial extracellular vesicles as promising nanocarriers for targeted therapy. *Extracellular Vesicles and Circular Nucleic Acids*, *3*, 63–86.

Luo, H., Li, X., Li, T., Zhao, L., He, J., Zha, L., Qi, Q., & Yu, Z. (2019). microRNA-423-3p exosomes derived from cardiac fibroblasts mediates the cardioprotective effects of ischaemic post-conditioning. *Cardiovascular Research*, *115*, 1189–1204.

Ma, J., Zhang, J., Wang, Y., Long, K., Wang, X., Jin, L., Tang, Q., Zhu, L., Tang, G., Li, X., & Li, M. (2018). MiR-532-5p alleviates hypoxia-induced cardiomyocyte apoptosis by targeting PDCD4. *Gene*, *675*, 36–43.

Mamtilahun, M., Jiang, L., Song, Y., Shi, X., Liu, C., Jiang, Y., Deng, L., Zheng, H., Shen, H., Li, Y., Zhang, Z., Wang, Y., Tang, Y., & Yang, G. Y. (2021). Plasma from healthy donors protects blood-brain barrier integrity via FGF21 and improves the recovery in a mouse model of cerebral ischaemia. *Stroke and Vascular Neurology*, *6*, 561–571.

Members, C.-N., and Partners. (2022). Database resources of the national genomics data center, china national center for bioinformation in 2022. *Nucleic Acids Research*, *50*, D27–D38.

Morente-Lopez, M., Fafian-Labora, J. A., Carrera, M., de Toro, F. J., Gil, C., Mateos, J., & Arufe, M. C. (2021). Mesenchymal stem cell-derived extracellular vesicle isolation and their protein cargo characterization. *Methods in Molecular Biology*, *2259*, 3–12.

Nobuta, T., Hirashima, S., Tada, N., Miura, T., & Itoh, A. (2011). One-pot metal-free syntheses of acetophenones from styrenes through aerobic photo-oxidation and deiodination with iodine. *Organic Letters*, *13*, 2576–2579.

Nunes, A. D. C., Weigl, M., Schneider, A., Noureddine, S., Yu, L., Lahde, C., Saccon, T. D., Mitra, K., Beltran, E., Grillari, J., Kirkland, J. L., Tchkonia, T., Robbins, P. D., & Masternak, M. M. (2022). miR-146a-5p modulates cellular senescence and apoptosis in visceral adipose tissue of long-lived Ames dwarf mice and in cultured pre-adipocytes. *Geroscience*, *44*, 503–518.

Oliveira, S., Cohen, R., Walsum, M. S., van Dongen, G. A., Elias, S. G., van Diest, P. J., Mali, W., & van Bergen En Henegouwen, P. M. (2012). A novel method to quantify IRDye800CW fluorescent antibody probes ex vivo in tissue distribution studies. *EJNMMI Research*, *2*, 50.

Pan, S., Pei, L., Zhang, A., Zhang, Y., Zhang, C., Huang, M., Huang, Z., Liu, B., Wang, L., Ma, L., Zhang, Q., & Cui, D. (2020). Passion fruit-like exosome-PMA/Au-BSA@Ce6 nanovehicles for real-time fluorescence imaging and enhanced targeted photodynamic therapy with deep penetration and superior retention behavior in tumor. *Biomaterials*, *230*, 119606.

Puzar Dominkus, P., Stenovec, M., Sitar, S., Lasic, E., Zorec, R., Plemenitas, A., Zagar, E., Kreft, M., & Lenassi, M. (2018). PKH26 labeling of extracellular vesicles: Characterization and cellular internalization of contaminating PKH26 nanoparticles. *Biochimica et Biophysica Acta. Biomembranes*, *1860*, 1350–1361.

Sano, H., Hsu, D. K., Apgar, J. R., Yu, L., Sharma, B. B., Kuwabara, I., Izui, S., & Liu, F. T. (2003). Critical role of galectin-3 in phagocytosis by macrophages. *Journal of Clinical Investigation*, *112*, 389–397.

Shi, X., Luo, L., Wang, J., Shen, H., Li, Y., Mamtilahun, M., Liu, C., Shi, R., Lee, J. H., Tian, H., Zhang, Z., Wang, Y., Chung, W. S., Tang, Y., & Yang, G. Y. (2021). Stroke subtype-dependent synapse elimination by reactive gliosis in mice. *Nature Communications*, *12*, 6943.

Shi, Y., Wang, X., Zhang, S., Yin, H., Fan, H., Tang, Y., & Yang, N. (2023). Research progress in in vivo tracing technology for extracellular vesicles. *Extracellular Vesicles and Circulating Nucleic Acids*, *4*, 684–697.

Song, Y., Li, Z., He, T., Qu, M., Jiang, L., Li, W., Shi, X., Pan, J., Zhang, L., Wang, Y., Zhang, Z., Tang, Y., & Yang, G. Y. (2019). M2 microglia-derived exosomes protect the mouse brain from ischemia-reperfusion injury via exosomal miR-124. *Theranostics*, *9*, 2910–2923.

Suo, Q., Deng, L., Chen, T., Wu, S., Qi, L., Liu, Z., He, T., Tian, H. L., Li, W., Tang, Y., Yang, G. Y., & Zhang, Z. (2023). Optogenetic activation of astrocytes reduces blood-brain barrier disruption via IL-10 in stroke. *Aging and Disease*, *14*, 1870–1886.

Tino, P. (2009). Basic properties and information theory of Audic-Claverie statistic for analyzing cDNA arrays. *BMC Bioinformatics*, *10*, 310.

Veziroglu, E. M., & Mias, G. I. (2020). Characterizing extracellular vesicles and their diverse RNA contents. *Frontiers in Genetics*, *11*, 700.

Wang, L., Feng, Z., Wang, X., Wang, X., & Zhang, X. (2010). DEGseq: An R package for identifying differentially expressed genes from RNA-seq data. *Bioinformatics*, *26*, 136–138.

Wang, Y., Liu, Y., Zhang, S., Li, N., Xing, C., Wang, C., Wang, J., Wei, M., Yang, G., & Yuan, L. (2023). Exercise improves metabolism and alleviates atherosclerosis via muscle-derived extracellular vesicles. *Aging and Disease*, *14*, 952–965.

Wang, Y. X. (2011). Superparamagnetic iron oxide based MRI contrast agents: Current status of clinical application. *Quantitative Imaging in Medicine and Surgery*, *1*, 35–40.

Welsh, J. A., Goberdhan, D. C. I., O'Driscoll, L., Buzas, E. I., Blenkiron, C., Bussolati, B., Cai, H., Di Vizio, D., Driedonks, T. A. P., Erdbrugger, U., Falcon-Perez, J. M., Fu, Q. L., Hill, A. F., Lenassi, M., Lim, S. K., Mahoney, M. G., Mohanty, S., Moller, A., Nieuwland, R., … Witwer, K. W. (2024). Minimal information for studies of extracellular vesicles (MISEV2023): From basic to advanced approaches. *Journal of Extracellular Vesicles*, *13*, e12404.

Wu, M., & Shu, J. (2018). Multimodal molecular imaging: Current status and future directions. *Contrast Media & Molecular Imaging*, *2018*, 1382183.

Wu, T., Song, H., Xie, D., Hua, K., Hu, J., Deng, Y., Ji, C., & Fang, L. (2020). Mir-30b-5p promotes proliferation, migration, and invasion of breast cancer cells via targeting ASPP2. *BioMed Research International*, *2020*, 7907269.

Xu, C., Pan, Y., Zhang, H., Sun, Y., Cao, Y., Qi, P., Li, M., Akakuru, O. U., He, L., Xiao, C., Sun, B., Bian, L., Li, J., & Wu, A. (2023). Platelet-membrane-coated polydopamine nanoparticles for neuroprotection by reducing oxidative stress and repairing damaged vessels in intracerebral hemorrhage. *Advanced Healthcare Materials*, *12*, e2300797.

Xu, F., Cheng, C., Xu, F., Zhang, C., Xu, H., Xie, X., Yin, D., & Gu, H. (2009). Superparamagnetic magnetite nanocrystal clusters: A sensitive tool for MR cellular imaging. *Nanotechnology*, *20*, 405102.

Yang, H., Zhang, L., & Wang, Q. (2021). MicroRNA-221-3p alleviates cell apoptosis and inflammatory response by targeting cyclin dependent kinase inhibitor 1B in chronic obstructive pulmonary disease. *Bioengineered*, *12*, 5705–5715.

Yang, Y., Zhang, L., Cai, J., Li, X., Cheng, D., Su, H., Zhang, J., Liu, S., Shi, H., Zhang, Y., & Zhang, C. (2016). Tumor angiogenesis targeted radiosensitization therapy using gold nanoprobes guided by MRI/SPECT imaging. *ACS Applied Materials & Interfaces*, *8*, 1718–1732.

Yuan, F., Chang, S., Luo, L., Li, Y., Wang, L., Song, Y., Qu, M., Zhang, Z., Yang, G. Y., & Wang, Y. (2018). cxcl12 gene engineered endothelial progenitor cells further improve the functions of oligodendrocyte precursor cells. *Experimental Cell Research*, *367*, 222–231.

Zhang, L., Su, H., Cai, J., Cheng, D., Ma, Y., Zhang, J., Zhou, C., Liu, S., Shi, H., Zhang, Y., & Zhang, C. (2016). A multifunctional platform for tumor angiogenesis-targeted chemo-thermal therapy using polydopamine-coated gold nanorods. *ACS Nano*, *10*, 10404–10417.

Zhang, L., Wu, Y., Yin, X., Zhu, Z., Rojalin, T., Xiao, W., Zhang, D., Huang, Y., Li, L., Baehr, C. M., Yu, X., Ajena, Y., Li, Y., Wang, L., & Lam, K. S. (2021). Tumor receptor-mediated in vivo modulation of the morphology, phototherapeutic properties, and pharmacokinetics of smart nanomaterials. *ACS Nano*, *15*, 468–479.

Zhang, M., Vojtech, L., Ye, Z., Hladik, F., & Nance, E. (2020). Quantum dot labeling and visualization of extracellular vesicles. *ACS Applied Nano Materials*, *3*, 7211–7222.

Zhang, X., Si, Z., Wang, Y., Li, Y., Xu, C., & Tian, H. (2021). Polymerization and coordination synergistically constructed photothermal agents for macrophages-mediated tumor targeting diagnosis and therapy. *Biomaterials*, *264*, 120382.

SUPPORTING INFORMATION

Additional supporting information can be found online in the Supporting Information section at the end of this article.

How to cite this article: Shi, X., Zhang, L., Wu, S., Zhang, C., Mamtilahun, M., Li, Y., Zhang, Z., Zuo, C., Cui, F., Li, W., Yang, G.-Y., & Tang, Y. (2025). A simple polydopamine-based platform for engineering extracellular vesicles with brain-targeting peptide and imaging probes to improve stroke outcome. *Journal of Extracellular Vesicles*, *14*, e70031. https://doi.org/10.1002/jev2.70031